Schürz *et al.*
Cell Communication and Signaling (2025) 23:323
https://doi.org/10.1186/s12964-025-02223-x

Cell Communication and Signaling

RESEARCH

Open Access

Quantitative characterisation of extracellular vesicles designed to decoy or compete with SARS-CoV-2 reveals differential mode of action across variants of concern and highlights the diversity of Omicron

Melanie Schürz[1,3†], Isabel Pagani[2†], Eva Klinglmayr[1,3,4], Heloisa Melo Benirschke[1], Martin Mayora Neto[5], Luis J. V. Galietta[6], Arianna Venturini[6], Nicoletta Pedemonte[7], Valeria Capurro[7], Sandra Laner-Plamberger[8], Christoph Grabmer[8], Essi Emminger[9], Martin Wolf[9], Marianne Steiner[1], Cyrus Kohlmetz[1], Niklas Mayr[1], Liliia Paniushkina[9], Katharina Schallmoser[8], Dirk Strunk[9], Hans Brandstetter[1], Martin Hintersteiner[10], Nigel Temperton[5], Elisa Vicenzi[2*] and Nicole Meisner-Kober[1,3*]

Abstract

Background The converging biology between enveloped viruses and extracellular vesicles (EVs) has raised interest in the application of engineered EVs as antiviral therapeutics. Following the recent COVID-19 pandemic, EVs engineered with either the ACE2-receptor or Spike-protein have been proposed as strategy to either decoy SARS-CoV-2, or to compete with its cell entry. For generic use as a platform for future pandemic preparedness, a systematic and quantitative comparison of both strategies is required to assess their limitations and benefits across different variants of concern.

Methods Here we generated EVs decorated with either the ACE2-receptor or the Spike-protein of (Wuhan)-SARS-CoV-2 and used single vesicle imaging for in-depth quantitative characterisation. These vesicles were then systematically tested for anti-viral activity across SARS-CoV-2 variants of concern using both, pseudotype and live virus cellular infection models including primary human bronchial and nasal explants.

Results Spike-protein EVs or ACE2-EVs recovered from transiently transfected HEK293T cells comprised only a small fraction of the EV secretome (5% or 20%, respectively) and were primarily derived from the plasma membrane rather than multivesicular bodies. Redirecting intracellular trafficking of the Spike protein by mutating its transmembrane or subcellular localisation domains did not increase the yields of Spike-EVs. Both types of vesicles inhibited SARS-CoV-2 (D614G) in a dose dependent manner with kinetics and immunohistochemistry consistent with an inhibition at the initial cell entry stage. ACE2-EVs were more potent than Spike-EVs and at least 500–1000 times more potent

†M. Schürz and I. Pagani contributed equally to this work.

*Correspondence:
Elisa Vicenzi
vicenzi.elisa@hsr.it
Nicole Meisner-Kober
nicole.meisner-kober@plus.ac.at
Full list of author information is available at the end of the article

than soluble antibodies in a pseudotype model. Surprisingly, ACE2-EVs switched from an inhibitory to an enhancer activity for the Omicron BA.1 variant whereas Spike-EVs retained their activity across all variants of concern.

Conclusions While our data show that both types of engineered EVs potently inhibit SARS-CoV, the decoy versus competition strategy may result in diverging outcomes when considering viral evolution into new variants of concern. While Spike-EVs retain their competition for receptor binding even against higher affinity viral Spike mutations, the formation of complexes between ACE2-EVs and the virus may not only result in inhibition by decoy. As EVs are actively internalised by cells themselves, they may shuttle the virus into cells, resulting in a productive alternative cell entry route for variants such as Omicron, that diverge from strict plasma membrane protease cleavage to the use of endosomal proteases for release of their genome.

Introduction

Severe Acute Respiratory Syndrome Coronavirus 2 (SARS-CoV-2) is a positive single-stranded RNA enveloped virus, member of the Coronaviridae family and it is the aetiological agent of Coronavirus Disease 2019 (COVID-19). The virus was first isolated in Wuhan, China, at the end of 2019 and since then has been spreading worldwide, causing one of the most severe pandemics experienced in human history [12, 66]. Although the virus with its mutated versions has lost some of its threat over time and the development of efficacious vaccines has marked a turning point, periodic surges in infection rates highlight a need for novel anti-viral agents. Especially compounds capable of blocking cell entry and replication of corona viruses could be of pivotal importance for those individuals at higher risk of severe COVID-19 complications, and in anticipation of future pandemics.

SARS-CoV-2 enters cells through the interaction of the Spike protein exposed on the mature virions with the Angiotensin converting enzyme 2 (ACE2) protein that is the primary receptor of SARS-CoV-2 [22, 60]. ACE2 is a zinc metallo-peptidase that belongs to the family of the dipeptidyl carboxydipeptidase with the catalytic domain exposed on the extracellular leaflet of the plasma membrane. Its main physiological function is the cleavage of angiotensin I and angiotensin II generated by renin and ACE enzymes, into angiotensin 1–9 and angiotensin 1–7, respectively, which are crucial for regulating blood pressure [19, 39]. On mature SARS-CoV-2 virions, the Spike protein is composed of two separate subunits, S1 and S2, non-covalently linked and formed from the precursor Spike protein by furin proteolytic cleavage within the virus-producing cells [69]. The S1 subunit binds to ACE2 through its Receptor Binding Domain (RBD) located at the apex of Spike when it is in the "up" conformation, whereas the S2 subunit anchors the Spike protein to the viral membrane [69]. Binding of S1 to ACE2 exposes an additional cleavage site on S2 to the proteolytic activity of either transmembrane protease serin 2 (TMPRSS2) at the cell surface, or cathepsin L in the endosomal compartment following ACE2-mediated endocytosis [25]. This cleavage promotes the disengagement of S1 from S2, enabling S2 to undergo conformational changes that promote its elongation and fusion with the cellular membrane.

Targeting the entry step of the virus life cycle represents one of the most attractive therapeutic interventions, as it can prevent the initiation of the virus replication and spread and can be targeted by molecules that do not require cell penetration. An initial strategy for treatment of infected individuals thus involved the use of human monoclonal antibodies (mAb) against the Spike protein [10]. However, this approach has been challenging due to the emergence of various variants of concern (VoCs) over the last four years of the pandemic. VoCs are characterized by mutations primarily in the Spike protein, that render the virus more infectious, thereby endowing the new variant with the advantage to replace the pre-existing ones [41]. Of particular note is the Omicron variant, which was detected for the first time in South Africa and Botswana in November 2021 [58]. Omicron is characterized by at least 30 mutations and has been rapidly evolving to gain contagiousness and to escape pre-existing immunity conferred by either prior infection or vaccination [6]. In addition, the neutralization activity of the current approved mAb is fading, thus posing a continuous need for new mAbs that target highly conserved regions of the Spike protein [61, 62]. In contrast to anti-Spike mAb, ACE2 targeted strategies bypass the continuous accumulation of new mutations in the Spike protein. ACE2 mimetics such as ACE2 ectodomain lacking the transmembrane domain (shACE2), its Fc-fusion form that overcomes the short half-life of shACE2 and their variants selected for higher affinity have been shown to block SARS-CoV-2 infection both *in-vitro* and in vivo in animal models [34, 35, 70]. Catalytically inactive forms of ACE2 mimetics have also proven to inhibit SARS-CoV-2 infection with the VoCs up to the delta variant [5, 23].

Another strategy to inhibit the interaction between Spike and ACE2 is the use of extracellular vesicles (EVs) decorated with ACE2 or Spike ligands on their surface. Like many viruses, EVs are lipid bilayer particles which

cells release into the extracellular space either by plasma membrane budding or exocytosis from endosome derived compartments [37]. EVs expose transmembrane proteins such as CD63, CD81, or CD9 on their surface in the same orientation as the producing cells and can be engineered to display peptides or proteins of interest on their surface. This is achieved by overexpression of target proteins in the producing cells, whereas their successful packaging into EVs depends on their subcellular localisation and interaction with sorting machineries [9, 75]. EVs engineered to expose ACE2 on their surface were shown to inhibit SARS-CoV-2 infection in vitro and in vivo in animal models [8, 14, 65]. Interestingly, naturally occurring EVs carrying ACE2 as a consequence of SARS-CoV-2 infection were also detected in the plasma of infected individuals and were successfully used to coagulate the virus in in vitro and in vivo infection models [14]. One advantage of this approach as compared with that of soluble ACE2 mimetics is the possibility to maintain the full receptor including the ACE2 neck domain, thereby mimicking a more physiological conformation that allows homodimerization and facilitates a better accommodation of the Spike protein. Furthermore, engineered EVs are hypothesised to carry several copies of the ACE2 receptor and may thereby have both, increased avidity and the propensity to simultaneously bind and neutralize several virions.

Additionally, it has been shown that after both, SARS-CoV-2 infection as well as mRNA vaccination, circulating EVs carrying the Spike-protein on their surface are produced even before the detection of neutralising antibodies [2]. Consistently, engineered lung epithelial EVs, decorated with the receptor-binding domain of the S-protein on their surface, showed promising results as alternative immunogens for vaccination after administration by inhalation [61, 62]. Additionally, S-protein decorated EVs were proposed as vehicles for targeted delivery of antiviral agents [18] and an antiviral activity was described in mouse models [7]. Since engineered EVs are thus attractive candidates for the development of novel antiviral therapeutics, the mechanisms, benefits and limitations of these two major paradigms need to be characterised more systematically and quantitatively.

In this study, EVs were engineered in order to decorate the surface with GFP-tagged versions of either the ACE2 (ACE2-EVs) or the Spike protein (S-EVs) from the initial Wuhan SARS-CoV-2 variant, quantitatively characterised at the single vesicle level. A systematic characterisation of these engineered EVs and their antiviral activity was done using a SARS-CoV pseudovirus assay as well as live virus infection models in cell lines and primary human bronchial and nasal explants. Thereby we quantify for the first time the antiviral potency of engineered EVs at the single vesicle level and systematically compare the differential activity of viral decoy versus competition across different SARS-CoV-2 variants.

Material and methods

Plasmids

Cloning of the mCherry tagged human CD63 mammalian expression construct was performed as described previously [9, 21]. Human ACE2 (NM_021804) tagged with turboGFP (tGFP) [16] in pCMV6 (ORIGENE #RG208442) and native SARS-CoV-2 S-Protein (2019-nCoV) tagged with GFPSpark (GFPsp) in pCMV3 (SinoBiological#VG40589-ACG) [51] were obtained commercially.

To generate S-Protein (VSV-G TM) $GFP_{sp,}$ the transmembrane (TM) and cytoplasmic domains of SARS-CoV-2 S-Protein were exchanged by those from Vesicular Stomatitis Virus G- Protein (VSV-G) in analogy to previous chimeric constructs for S-protein from SARS-CoV-1 described by [28]. Four overlapping gene fragments were created as follows: Plasmid #VG40589-ACG was digested via XbaI/KpnI and served as a vector backbone (fragment 1). S-Protein sequence spanning aa1-1213 (fragment 2) and the sequence of GFP_{sp} including a GS linker (fragment 4) were PCR amplified from plasmid #VG40589-ACG. The VSV-G TM sequence spanning aa441-511 (GenBank accessionM35219.1) was purchased as Gene Strands from Eurofins Genomics (fragment 3). Primers and the Gene Strands were designed to overlap with the adjacent fragment or vector backbone and were assembled via HiFi DNA Assembly using NEBuilder HiFi DNA Master Mix (NEB).

S-Protein (ΔERGIC) GFPsp constructs were generated by deleting the ERGIC (Endoplasmic Reticulum Golgi-Intermediate Compartment) localisation signal (aa1269-1273) in analogy to [31]. Cloning was performed as described above via HiFi DNA assembly using the following fragments: Fragment 1 was created as described above. PCR-amplified sequences spanning S-Protein aa 1–1268 (2) and the GFP_{sp} sequence including a GS linker (3) were PCR amplified from plasmid #VG40589-ACG. All primers and constructs are listed in Supplementary File 1.

Cell lines

The Vero cell line was obtained from the Instituto Zooprofilattico of Brescia, Italy (BS CL101), and ATCC (CCL-81), respectively and was cultivated in Eagle's minimum essential medium (EMEM; Lonza) supplemented with 10% fetal bovine serum (FBS; Euroclone) 1% penicillin–streptomycin and 1% glutamine.

HEK293T/17 cells (ATCC CRL 11268) were maintained in Dulbecco's Modified Eagle's Medium High

Glucose (DMEM; Pan Biotech P04-04510) supplemented with 10% FBS (Pan Biotech P40-37500HI) and 1% penicillin and streptomycin (Pan Biotech P06-07100). CHO cells (ATCC CCL 61) were maintained in Ham F12 (Pan Biotech P04-14500) supplemented with 10% FBS (Pan Biotech P40-37500HI), and 1% penicillin streptomycin (Pan Biotech P06-07100). CHO-ACE2-TMPRSS2 cells were maintained in Ham F12 (Pan Biotech P04-14500) supplemented with 10% FBS (Pan Biotech P06-07100), 1% penicillin–streptomycin (Pan Biotech P06-07100), 2 µg/mL Puromycin (Merck-Millipore 540,411-25MG) and 100 µg/mL Hygromycin (Merck-Millipore 400,050–100MG). The human lung epithelial Calu-3 cell line was obtained from NovusPharma and was cultivated in DMEM supplemented with 20% FBS, 1% penicillin–streptomycin, 1% glutamine, 1% non-essential amino acids and 1% sodium pyruvate.

The human embryonic kidney (HEK293T; CRL-3216) cell line, kindly provided by the group of Prof. Dr. H. Brandstetter (Paris Lodron University Salzburg, Austria) was cultivated in DMEM (Gibco, MD, USA) supplemented with 10% fetal bovine serum (FBS, Gibco, MD, USA), 1% GlutaMAX Supplement 100x (Gibco, MD, USA) and 1% Antibiotic/Antimycotic (100x, Gibco, MD, USA).

HEK293T cells stably transfected with CD63–mNeon were kindly provided by Dr. Samir El Andaloussi and Dr. Andre Görgens (Karolinska Insitute, Stockholm, Sweden [9, 11] and were cultivated in DMEM (Gibco, MD, USA) supplemented with 10% fetal bovine serum (FBS, Gibco, MD, USA), 1% GlutaMAX Supplement 100x (Gibco, MD, USA) and 1% Antibiotic/Antimycotic (100x, Gibco, MD, USA).

All cell lines were incubated at 37 °C, 5% CO_2 and 90% relative humidity.

Human Bronchial Epithelial Cells (HBEC)

The isolation, culture, and differentiation of primary human bronchial epithelial cells (HBECs) were done as previously reported [49], with some modifications. Briefly, epithelial cells were harvested from the mainstem bronchi of individuals undergoing lung transplants. For this study, cells were obtained from four donors (BE37, BE63, BE168 and BE177; see Table 1). The epithelial cells were detached by treating the bronchi overnight with protease XIV and then cultured in a serum-free medium (LHC9 mixed with RPMI 1640, 1:1) supplemented as described [49]. The collection and study of bronchial epithelial cells for investigating airway epithelium physiopathology were specifically approved by the Ethics Committee of the Istituto Giannina Gaslini in accordance with the guidelines of the Italian Ministry of Health (registration number: ANTECER, 042–09/07/2018).

Table 1 Human bronchial epithelial cell donors

Donor ID	Diagnosis	Sex	Age*
BE37	Pulmonary hypertension	M	-
BE63	Idiopathic pulmonary fibrosis	F	63
BE168	Pulmonary fibrosis	M	55
BE177	Pulmonary fibrosis	M	64

Informed consent was obtained from each patient using a form previously approved by the Ethics Committee.

To obtain differentiated epithelia, cells were seeded at a high density (5×10^5 cell/snapwell) on 12-mm diameter porous membranes (Snapwell inserts, Corning, code 3801). After 24 h, the serum-free medium was removed from both sides and replaced only on the basolateral side with Pneumacult ALI medium (StemCell Technologies). The cells were then differentiated for 3 weeks under in air–liquid interface (ALI) conditions.

Human Nasal Epithelial Cells (HNEC)

Air–liquid interface human nasal epithelial cells (hNECs) were purchased from Epithelix and maintained in Mucilair cell culture medium (Epithelix). Pooled nasal epithelial cells from 14 individual donors were then seeded on 6.5-mm Transwell® inserts (cat #3470, Corning Incorporated, Oxyphen, Wetzikon, Switzerland) in MucilAir™ culture medium (EP04MM, Epithelix Sàrl, Geneva, Switzerland). Once confluent, air–liquid interface (ALI) was established and maintained for at least 28 days for mucociliary differentiation. Average culture time post ALI was 43 days.

Patient sera

Whole blood donations were collected at the Department for Transfusion Medicine of the University Hospital Salzburg, Austria. All donors had a brief health screening and completed a written questionnaire prior to blood donation, including an informed consent on pathogen screening as part of further processing and on the use of leftover material for research purposes. All samples were screened negative for the infectious disease parameters HIV1/2, HAV, HBV, HCV, PB19 and syphilis. In addition, screening for anti-SARS-CoV-2 anti-N total antibody (including IgM, IgG and IgA) using the Elecsys Anti-SARS-CoV-2 (ACOV2) total antibody electrochemiluminescence immunoassay (ECLIA, Roche Diagnostics, Basel, Switzerland) on a Cobas8000-e801 device (Roche Diagnostics) was done as described in [38]. Three anti-SARS-CoV-2 anti-N negative serum pools, each containing serum of 50 individuals, were used as negative controls (see also Supplementary Table 1).

COVID-19 convalescent serum

In the course of the COVID-19 pandemic, plasma products of convalescent donors were collected at the Department of Transfusion Medicine by apheresis (Trima Accel cell separator, Terumo BCT, Lakewood, CO, USA) for transfusion of critically ill patients, as described in [29]. The donors had to be fully recovered at least for four weeks from COVID-19 infection, confirmed by RT-qPCR and SARS-CoV-2 anti-N antibody screening. After clinical evaluation, negative screening for infectious diseases, normal range of plasma protein, immunoglobulins, creatinine and full blood count as well as positive testing for anti-SARS-CoV-2 antibodies, plasma donation was permitted. In the frame of apheresis, additional 7 mL of serum was collected from one male donor (age 26 years) after written informed consent (approved by the Ethics Committee Salzburg, vote 1080/2020), and frozen at—80 °C until use. As shown in Supplementary Table 1c, two different assays were applied for anti-SARS-CoV-2 screening according to manufacturer's instructions: the Elecsys Anti-SARS-CoV-2 total anti-N antibody ECLIA (Roche Diagnostics) and a SARS-CoV-2 Surrogate Virus Neutralization Test (sVNT) (GenScript, Piscataway Town-ship, New Jersey, USA) using an ETIMax3000 platform (Diasorin, Saluggia, Italy).

Pseudovirus production

Pseudotype viruses were produced in HEK293T/17 cells pre-seeded in a T175 flask (Thermo) with approximately 5×10^6 cells the day before transfection. Cells were then co-transfected with 2 µg of packaging lentiviral core p8.91, 3 µg of pCSFLW encoding Firefly luciferase, and 2 µg of the Spike SARS2 (D614G)-pCAGGS (Medicines & Healthcare Products Regulatory Agency CFAR100985), SARS pCAGGS, and Omicron (BA.1) in pcDNA3.1 se using FugeneHD (Promega) transfection reagent at a ratio of 1:3 DNA:FugeneHD in OptiMEM (Gibco). After a 15 min incubation at room temperature, the transfection mix was added to the cell culture media. PVs were harvested at 48 h post transfection and supernatant filtered through a 0.45 µm cellulose acetate filter (Starlab).

Extracellular vesicle production and characterisation

For EV production (S-GFP_{sp} EVs, ACE2 tGFP EVs), 2×10^7 human embryonic kidney cells (HEK293T) were seeded in T225 cell culture flasks, left to attach overnight, washed with OptiMEM (Gibco, MD, USA) and then transfected with plasmids of interest by preparing DNA complexes with branched polyethyleneimine (Sigma, MO, USA; 60 µg DNA: 90 µg PEI). 4 h after transfection, the medium was changed to OptiMEM supplemented with 1% antibiotic/antimycotic. Conditioned medium (CM) was harvested after 48 h of cultivation. For EV production from native HEK293T cells or from the stably expressing CD63- mNeon line, cells were seeded in T225 or 3 layered T175 flasks (with 2×10^7 or 4×10^7 cells each) and left to attach overnight. After washing with OptiMEM, the cells were incubated in OptiMEM supplemented with 1% Antibiotic/Antimycotic and the CM was harvested after 48 h.

For EV isolation, conditioned medium from transiently transfected and native HEK293T cells was collected and centrifuged twice at 300 ×*g* for 5 min and once at 3000 ×*g* for 15 min. After filtration through a 0.22 µm filter, the CM was concentrated 50–100 ×via ultrafiltration (UF) using a 200 mL Amicon Stirred Cell over a 100 kDa MWCO filter. The flow-through of the UF step was collected, filtered through a 0.22 µm membrane and used as a negative control termed "soluble fraction" throughout the manuscript (matched by total protein concentration). The concentrate of the UF was further filtered through a 0.22 µm membrane and 1 ml was loaded on a Superdex 200 Increase 10/30GL column (GE Healthcare, IL, USA) for chromatography on a Shimadzu LC-20 AI FPLC instrument equipped with a SPD-M20 A Photodiode Array Detector (Shimadzu, Japan) and a RF-20 A Fluorescence Detector (Shimadzu, Japan). The sample was eluted under isocratic conditions at 4 °C and 0.8 mL/min using phosphate buffered saline (PBS: 8 g NaCl, 0.2 g KCl, 1.44 g Na_2HPO_4, 0.24 g KH_2PO_4 per litre) adjusted to a pH of 7.4 and further filtered through a 0.22 µm filter. Fractions were pooled as indicated in Supplementary Fig. 1a and concentrated to a concentration of $>1*10^{12}$ particles/ml (measured by NTA) with a 10 kDa MWCO Amicon Ultra 4 mL centrifugal filter. The EV samples were stored at 4 °C until further use.

Protein concentration determination

Protein concentrations were determined by Bradford measurements using the Pierce Detergent Compatible Bradford Assay Kit (Thermo Fisher Scientific, MA, USA) following the manufacturer's instructions. Absorbance at λ_{max} = 595 nm was measured on a NanoDrop 2000c Spectrophotometer (Thermo Scientific, MA, USA).

Nanoparticle tracking analysis

Particle size distributions and concentrations were determined by nanoparticle tracking analysis (NTA) on a Nanosight LM14 C equipped with a 488 nm laser (Malvern, UK) using the NTA analytical software version 3.1.54. Samples were diluted in their respective buffer and five videos (1 min each) were recorded with a camera level of 13–15, screen gain 1. Analysis software settings were kept constant for all measurements (detection

threshold 5). For each sample, the mean of three individual measurements was calculated.

Analytical FPLC-SEC

Size exclusion chromatography (SEC) experiments were performed on a Shimadzu custom built system comprised of a mobile phase degassing unit (Shimadzu DGU-20 A3R), three liquid chromatography pumps (Shimadzu Prominence LC-20 Ai) a PDA detector (Shimadzu SPD-M20 A) and a Fluorescence detector (Shimadzu RF-20 A) with automated fraction collection (Shimadzu FRC-10 A). The chromatographic system was mounted in a cold cabinet (Tritec, Hannover, DE) to ensure a constant temperature of 4 °C during the runs. The Shimadzu LabSolutions software 5.97 was used for data acquisition, GraphPad Prism 9.1.2 was used for data analysis. For analytical size exclusion chromatography of conditioned medium, CM was harvested from transfected cells, as described above, centrifuged twice at 300 ×*g* for 5 min and once at 3000 ×*g* for 15 min and filtered through a 0.22 µm membrane. CM (1 mL injection volume) was fractionated on a dextran-agarose matrix column (Superdex® 200 Increase 10/300 GL, L× I.D. 30 cm ×10 mm, 8.6 µm) with isocratic elution at a flow of 0.8 mL/min. All samples were monitored by detection of the UV absorbance at 280 nm and simultaneous fluorescence detection as specified in the chromatograms.

Immunofluorescence for single vesicle imaging

Immunofluorescence for single vesicles imaging was performed according to [48]. Briefly, 1× 10^9 particles/ml of UF SEC purified EV solution were immobilised on quartz glass microscope slides by 30 min incubation of the EV solution in a humidified chamber. Then EVs were fixed with 4% PFA, blocked with normal goat serum (NGS) and incubated with primary antibodies in 1% NGS blocking buffer as specified for each experiment (anti-CD9 (Ms mAb to CD9 [MM2/57], Invitrogen) (1:1000); anti-CD63 (Ms mAb to CD63 [TS63], Thermo Fisher) (1:1000); anti-CD81 (Ms mAb to CD81 [1D6], Bio Rad) (1:1000); anti SARS-CoV-2 Spike antibody (Ms mAb to SARS-CoV-2 (COVID-19) Spike antibody [1 A9], GeneTex (1:100)) followed by incubation for 1 h at RT with secondary antibody (anti-Mouse AF555 (Goat pAb to Ms IgG Alexa Fluor 555, Abcam) diluted 1:1000 in PBS.

Single vesicle imaging with patient sera was performed as described above for immunofluorescence using commercial antibodies, whereas serum from COVID-19 positive or COVID-19 negative donors (diluted 1:5 in PBS) served as primary antibody and anti-Human Alexa Fluor Plus 555 (Goat Ab to Hm IgG (Alexa Fluor 555), A4827, Thermo scientific) diluted 1:1000 in PBS was used as a secondary antibody.

Samples were embedded in Vectashield Antifade mounting medium (Vector laboratories, H-1000) and stored at RT protected from light until imaging. Single vesicle imaging of EVs immobilised directly from conditioned medium was performed by incubation of 35 µl of CM on quartz glass microscope slides for 30 min in a humified chamber followed by embedding in PBS.

Post isolation labelling of EVs with Cy5-NHS

1 ml of UF-SEC purified native, S-GFP$_{sp}$, ACE2-tGFP or CD63-mNeon EVs at a concentration of 6*10^{11} particles/ml (1 nM) were incubated with 10 µM Cy5 – NHS ester (lumiprobe (Germany) CAS No.: 1263093–76-0) at 37 °C for 1 h with shaking at 1500 rpm. Free dye was removed by FPLC – SEC on a Superdex 200 Increase 10/30 GL column (GE Healthcare). Chromatograms were recorded using a UV/VIS absorbance diode array detector (DAD) as well as simultaneous recording of GFP/mNeon fluorescence (488/510 nm or 504/517 nm ex/em, respectively) and Cy5 fluorescence (646/662 nm ex/em) in a split detection mode on the fluorescence detector. EV fractions were pooled and analysed by single vesicle imaging.

Cell uptake of EVs

Vero cells were seeded at 5× 10^4 cells/mL with 300µl per well into a 96-well µ-plate (Ibidi (WI, USA); 300 µL/well) pre-coated for 1 h with 20 µg/mL fibronectin from human plasma (Sigma Aldrich, MO, USA) diluted in PBS. Cells were allowed to attach by incubation in DMEM (Gibco, MD, USA) supplemented with 10% FBS (Gibco, MD, USA) and 1% of a 100 ×antibiotic/antimycotic solution (Gibco, MD, USA) at 37 °C, 5% CO_2 and 90% relative humidity overnight. The next day the medium was changed to medium containing different concentrations of fluorescently labelled EVs (determined by NTA) as indicated. After 3 h, the cells were washed once with medium and fixed with Pen-Fix (Thermo Scientific, MA, USA) supplemented with 0.1 µg/mL Hoechst for 20 min and subsequently washed 3 times with PBS, pH 7.4 (Gibco, MD, USA). Fixed cells were kept in 1× PBS in sealed plates and stored at 4 °C.

High- resolution wide field fluorescence microscopy

Cellular and single vesicle imaging was performed on an Olympus IX83 microscope equipped with spectral filters for DAPI, GFP, Cy3, Cy5 and Cy7 and five different objectives. For imaging of EV cell uptake a 40 ×objective (UPLXAPO40X NA 0.95) and a hardware autofocus (IX3-ZDC2-830 Z Drift Compensation) enabling automated plate scanning were used. For imaging based high content single vesicle characterisation, a 100 ×oil objective (UPLXAPO100XO NA1.45) was used. A SPECX7IR-LFIB Light Engine (Lumencor) was used as

excitation light source with 6 LEDs and additional excitation filters for the following wavelengths: 395/25 nm, 438/29 nm, 475/28 nm, 555/28 nm, 575/25 nm, 635/22 nm and 730/40 nm. Either a Penta-Band dichroic mirror (AHF-SPX-PSEM) or specific emission filter cubes for the respective fluorophores were used in the optical path (49,002—ET—EGFP filter cube: ET470/40 ×EX and ET525/50 m EM; 49,004—ET- CY3/TRITC filter cube: ET545/25 ×EX and ET605/70 m EM).

Image processing and analysis

All images shown side by side are recorded with similar exposure times and are shown to scale. Cellular localisation of the spike protein and the ACE2 protein with and without CD63 mCherry (Fig. 2) is shown as single stack out of a Z-stack after deconvolution. Single vesicle imaging (Fig. 3, 4 and 5) is performed using a 40 ×or a 100 ×objective and images. Unprocessed images are analysed using the "coloc" function of the Fiji plugin EVAnalyzer [48]. EV uptake into cells (Fig. 5) was monitored after cell fixation and images were recorded as Z-stack. Deconvolution of images, using the constrained iterative deconvolution plugin of the Olympus "Cell Sense dimension" software was performed, and a Maximum intensity projection (MIP) of the image was generated. Images were analysed using the "EV count per cell- remove cropped " function of the Fiji plugin EVAnalyzer.

Super resolution microscopy

To obtain sub-diffraction limit resolution images of single EVs, 1×10^9 EVs in 1 µL were stained with an anti-CD63, (Becton Dickinson, USA) or an anti- CD81 (R&D Systems, USA) antibody conjugated to Alexa Fluor 647, as described [64]. To immobilize stained EV Samples, the ONI EV profiler kit (Oxford Nanoimaging, United Kingdom) was used according to manufacturer's instructions. In brief, the glass surface of the provided microfluidic chip was functionalized with proprietary EV binding chemistry. After washing, EVs were loaded on the chip and fixed with fixation buffer. For imaging, microfluidic channels containing the immobilised EVs were loaded with BCubed super resolution imaging buffer (Oxford Nanoimaging, United Kingdom), which enhances fluorophore blinking and prevents photobleaching. Three fields of view were recorded for each sample using direct stochastic optical reconstruction microscopy (dSTORM) on a Nanoimager S instrument (Oxford Nanoimaging, UK) using 40%, 20% and 20% power for the 488 nm, 561 nm and 640 nm lasers, respectively. For localisation mapping, 2500 images were recorded per channel.

NanoFCM measurement

NanoFCM (High Sensitivity Flow Cytometry for Nanoparticle Analysis) was performed on a nanoFCM flow nano-analyzer (NanoFCM Co.) following the manufacturer's instructions to measure particle concentration and size. Briefly, the instrument applies two single photon-counting avalanche photodiodes (APDs) for simultaneous detection of side scatter (SSC) and fluorescence of particles, which was used to determine the ratio of vesicles with and without a GFP for S-GFP_{sp} EVs and ACE2-tGFP EVs. The instrument was calibrated separately for concentration and size using 200 nm polystyrene beads and a silica nanosphere cocktail (provided by nanoFCM as pre-mixed silica beads with diameters of 68, 91, 113, and 151 nm currently called as NanoFCM Quality Control Nanospheres), respectively. 20 µl of each EV preparation were diluted by sterile PBS in a range from 1:10 to 1:2000 allowing to detect at least 500 particles. Events were recorded for 60 s for each biological sample twice. The flow rate and side scatter intensities were converted into corresponding particle concentrations and size using the nanoFCM software.

Transmission electron microscopy

Sample preparation for negative staining was performed by dropping 10 µl EV solution (concentration of 2×10^{10} to 10^{11} particles/mL) onto Formvar carbon coated 200 mesh TEM grids (Agar Scientific, Essex, UK), which were fixed between tweezers. The solution was concentrated on air at room temperature for 30–45 min and excess liquid was removed with a filter paper. EVs were washed 3× using 100 µl of ddH_2O and fixed with 1% (v/v) glutaraldehyde in PBS followed by 8 washing steps in ddH_2O. Negative staining was then performed using aqueous 2% (w/v) uranyl acetate for 5 min followed by (flat) air-drying for an hour. Specimens were imaged on a transmission electron microscope Leo EM 910 (Zeiss, Oberkochen, Germany). Micrographs were taken on a Tröndle Sharp:eye digital camera.

Western blotting

Samples (Cell lysates, SolF, EVs or recombinant SARS-COV-2 (R&D systems biotechne 10,549-CV) as indicated) were mixed with SDS reducing buffer separated on 4–20% TGX Gels (BioRad) under non-reducing (CD9, CD63, CD81 and serum) or reducing conditions in an SDS containing Electrode running buffer at pH 8.3. Proteins were transferred onto a 0.45 µM nitrocellulose or PVDF-membrane by semi dry blotting in a transfer buffer containing 10% methanol. Then the membrane was blocked with either TBS supplemented with 0.2% Tween and 2% BSA (for WB with human sera) or with

0.05% Tween and 2% BSA (for WB with commercial antibodies) for 1 h at room temperature. The blots were incubated with primary antibodies (CD63: Thermo Scientific 10628D (1:1000); ACE2: abcam ab15348 (1:5000); CD9: Invitrogen AHS0902 (1:2000); CD81: Bio-Rad MCA1847 (1:10 000); Flotillin-1: BD 610821 (1:1500); SARS-CoV-2 Spike glycoprotein: abcam ab272504 (1:1000); TMPRSS2: abcam ab92323 (1:500); Calnexin: Cell signaling #2679 (1:1000); human serum; GeneTex SARS-CoV/SARS-CoV-2 [1 A9]: SZABO-SCANDIC GTX632604-100 (1:2000), Serum from COVID-19 negative and COVID-19 reconvalescent patients (1:100)), diluted in the respective blocking buffer, overnight at 4 °C on the shaker. Secondary antibodies (Goat anti-Human IgG Cross-Adsorbed Secondary Antibody, HRP; (Invitrogen #62–8420; 1:4000); Rabbit anti-mouse IgG-HRP (Cell Signaling #7076; 1:3000), anti-rabbit HRP) (ab6112; 1:20.000), diluted in the respective blocking buffers, were incubated with the membranes for 1 h. Washing steps after primary and secondary antibody incubations were performed 5 times each with TBS + 0.2% Tween or TBS + 0.05% Tween for 5 min. The blots were imaged with the Licor system for fluorescence (Licor Odyssey FC Model 2800; with an image) or on a Biorad system (ChemiDoc XRS +) for chemiluminescence detection, depending on the secondary antibody.

Pseudovirus transduction experiments

EVs, human convalescent serum or monoclonal antibodies (NanoTools) were serially diluted in Ham F12 medium to achieve the required concentrations in a white 96-well F-bottom plate (Thermo). PV were diluted to achieve 10^5–10^6 relative light units per well before adding to the plate and incubating at 37 ˚C for 1 h. Target cells (CHO or CHO ACE2 TMPRSS2) were then added (10^4 cells per well) and incubated at 37 ˚C for 48 h. Cells were lysed with Bright Glo reagent (Promega) and luminescence was measured using a GloMax Navigator luminometer (Promega).

SARS-CoV-2 and SARS-CoV-1 viral isolates

The isolation of viruses from clinical samples and their subsequent use in research was approved by the IRCCS San Raffaele Scientific Institute Review Board as part of the COVID-19 Biobanking project 'COVID-Biob' (34/int/202019 March 2020; ClinicalTrials.gov Identifier: NCT04318366). Informed consent was obtained from each participant.

The SARS-CoV-2 isolate of the B.1 lineage with the Spike D614G mutation (GISAID accession ID: EPI_ISL_413489) was derived from the nasopharyngeal swab of a mildly symptomatic patient by inoculation of Vero E6 cells as previously described (Clementi, N. et al., 2020; Mycroft-West, C. J. et al. 2020; Stravalaci M. et al., 2021). The isolate of the South African B.1.351 (b) lineage (GISAID accession ID: EPI_ISL_1599180) was obtained an Italian 80-year-old male patient. The isolate of the B.1.1.7 (a) lineage (GISAID accession ID: EPI_ISL_1924880) came from an Italian 58-year-old female patient. The P.1 (g) lineage isolate (GISAID accession ID: EPI_ISL_1925323) was sourced from an Italian 43-year-old female patient. Lastly, the B.1.617.2 (d) lineage (GISAID accession ID: EPI_ISL_4198505) was obtained from an Italian 50-year-old male patient. The SARS-CoV-2 isolate of the B.1.1.529 + BA (Omicron) lineage (GISAID accession ID: EPI_ISL_12221510) was derived from an Italian 53-year-old female patient.

Secondary viral stocks were generated by infecting adherent Vero cells seeded in a 25 cm^2 tissue culture flask with 0.5 ml of the primary isolate diluted in 5 ml of complete medium. Three days post- infection, the culture supernatant was harvested, centrifuged and passed through a 0.45 µm filter. These secondary SARS-CoV-2 aliquots were maintained at −80 °C. Viral titres were determined using a plaque-forming assay.

The SARS-CoV-1 HSR isolate was originally obtained in 2003 from a sputum sample collected from an Italian man who had returned from Vietnam with atypical pneumonia, as previously described [40, 59].

Infections

Vero cell infection

Vero cells were plated at 2.5×10^5 cells per well in 24-well plates (Corning) and cultured with complete medium. After 24 h, the cells were treated with ten-fold serial dilutions of extracellular vesicles (Empty-EVs, S-EVs, ACE2-EVs) together with 50 PFU of SARS-CoV-2. After 1 h of incubation, the viral inoculum was removed, and cells were covered with 500 µl of 1% methylcellulose (Sigma) dissolved in EMEM supplemented with 1% FBS. Seventy-two hours post-infection (PI), the cells were stained with 1% crystal violet (Sigma) in 70% methanol.

Calu-3 cell infection

Calu-3 cells were seeded in 48-well plates (Corning) at a density of 5×10^4 cells per well in complete medium, 24 h before infection. 10^{11} EVs were added together with SARS-CoV-2 containing supernatant to obtain a multiplicity of infection (MOI) of 1 in a final volume of 250 µl of DMEM supplemented with 2% FBS. After 1 h of viral adsorption, the inoculum was removed and replaced with complete medium. Culture supernatants were collected at 24, 48 and 72 h PI and stored at – 80 °C until viral titres were determined by a plaque-forming assay in Vero cells.

HBEC and HNEC Infection

Forty-eight hours before infection, the apical surface of HBEC was washed with 500 µl of HBSS for 1.5 h at 37 °C, and the cultures were transferred to fresh air–liquid interface medium. Immediately before infection, to remove accumulated mucus production, the apical surfaces were washed twice with 500 µl of HBSS, with each wash lasting 30 min at 37 °C. Following the washes, 10^{11} EVs were added to the apical surface in 100 µl of HBSS along with the viral inoculum (SARS-CoV-2) at a MOI of 1. HBEC were incubated for 2 h at 37 °C. Afterward, the viral inoculum was removed, and the apical surface was washed three times with 500 µl of PBS. The cultures were maintained at 37 °C for 72 h PI. Infectious viruses were collected from the apical surface wash of the culture with 100 µl of PBS every 24 h up to 72 h PI, stored at − 80 °C until analysis, and later titre using a plaque assay in Vero cells. At 72 h PI, the cells were fixed in 10% formalin overnight at 4 °C for immunofluorescence analysis.

All infection experiments were conducted in a biosafety level 3 (BSL-3) laboratory at IRCCS San Raffaele Scientific Institute.

Protease inhibitor testing

Calu-3 cells were seeded in 48 well plates at the concentration of 5×10^4 cell/well. After 24 h, cells were pretreated for 1 h with either Camostat or E64D inhibitors at a concentration of 10 or 100 µM. After pretreatment, EVs were added at a concentration of 10^{11} together with SARS-CoV-2 VoCs (D614G or Omicron BA.1.) containing supernatant to obtain an MOI of 1 in a final volume of 250 µl of DMEM supplemented with 2% FBS. After 1 h of viral adsorption, the inoculum was removed and replaced with complete medium. 72 h post infection, cell culture supernatants were collected and stored at − 80 °C until determination of the viral titers by a plaque-forming assay in Vero cells.

Plaque-forming assay

The viral titres of SARS-CoV-2 isolates were measured in a plaque-forming assay optimized for Vero cells. Confluent Vero cells (1.5×10^6 cells/well) were seeded in 6-well plates (Corning) and incubated in duplicate with 1 ml of EMEM supplemented with 1% FBS containing tenfold serial dilutions of the viral stocks. After 1 h of incubation, the viral inoculum was removed, and 1 ml of methylcellulose (dissolved in EMEM supplemented with 1% FBS) was overlaid onto each well. After 72 h of infection, the cells were stained with 1% crystal violet (Sigma) in 70% methanol. Plaques were counted using a stereoscopic microscope (SMZ-1500; Nikon Instruments) and virus titres were calculated in terms of plaque forming units (PFU)/ml.

To determine the viral titres in supernatants collected from Calu-3 and HBEC cells, confluent Vero cells (2.5×10^5 cells/well) were seeded in 24-well plates (Corning) 24 h prior to infection. The cells were incubated with 300 µl of EMEM supplemented with 1% FBS containing 1:10 serial dilutions of virus-containing supernatants. The plaque-forming assay was performed as described above.

Immunocytochemistry

After washing in PBS, the epithelia were processed for antigen retrieval using 10 mM citrate buffer (pH 6), heated to 95 °C for 5 min. Then, all epithelia were permeabilized with 0.1% PBS-Triton X-100 for 10 min and subsequently blocked with 5% milk powder in 0.01% PBS-Tween (blocking solution) for 1 h at room temperature. Primary antibodies, diluted in the blocking solution, were incubated for 1 h at room temperature. The following antibodies were used: mouse IgG2a anti-dsRNA J2 (Scicons, # 10,010,500); mouse IgG1 anti-SARS-CoV-2 Nucleocapsid (Sino Biological, # 40,143-MM05); mouse IgG1 anti-SARS-CoV-2 spike (Genetex, GTX632604-100), all diluted 1:1000. Ciliated cells were stained with a mouse IgG2b anti-acetylated tubulin antibody (7451, Sigma-Aldrich) diluted 1:300. After three washes in 0.01% PBS-Tween, the epithelia were incubated with Alexa Fluor secondary antibodies (Thermo Fisher Scientific) at 1:200 dilution in the blocking solution for 45 min at room temperature in the dark. Following another three washes, the porous membrane carrying the epithelium was cut from the Snapwell's plastic support and mounted on microscope slides. Samples were mounted with Fluoroshield containing DAPI (Sigma-Aldrich) to stain cell nuclei. Imaging was performed using a Leica SPE confocal microscope system. Confocal images were acquired in xyz planes with 40X objective..

Graphs Illustrations and statistics

Graphs and statistics were generated using GraphPad Prism 9.1.2 with statistical testing performed as specified in each figure legend. Illustrations were created in Biorender.

Results

Engineering of HEK293T EVs decorated with ACE2, or SARS-CoV-2 Spike protein on the surface

Engineered EVs were designed to inhibit viral entry by either decoy or competition with Spike binding to the ACE2 receptor of recipient cells by decoration with either ACE2 or Spike protein on the EV surface (Fig. 1a). Surface decorated EVs were generated by transient overexpression of the ACE2 or Spike proteins in the producing cells cultured in serum-free OptiMEM, followed by UF-SEC purification from the conditioned medium

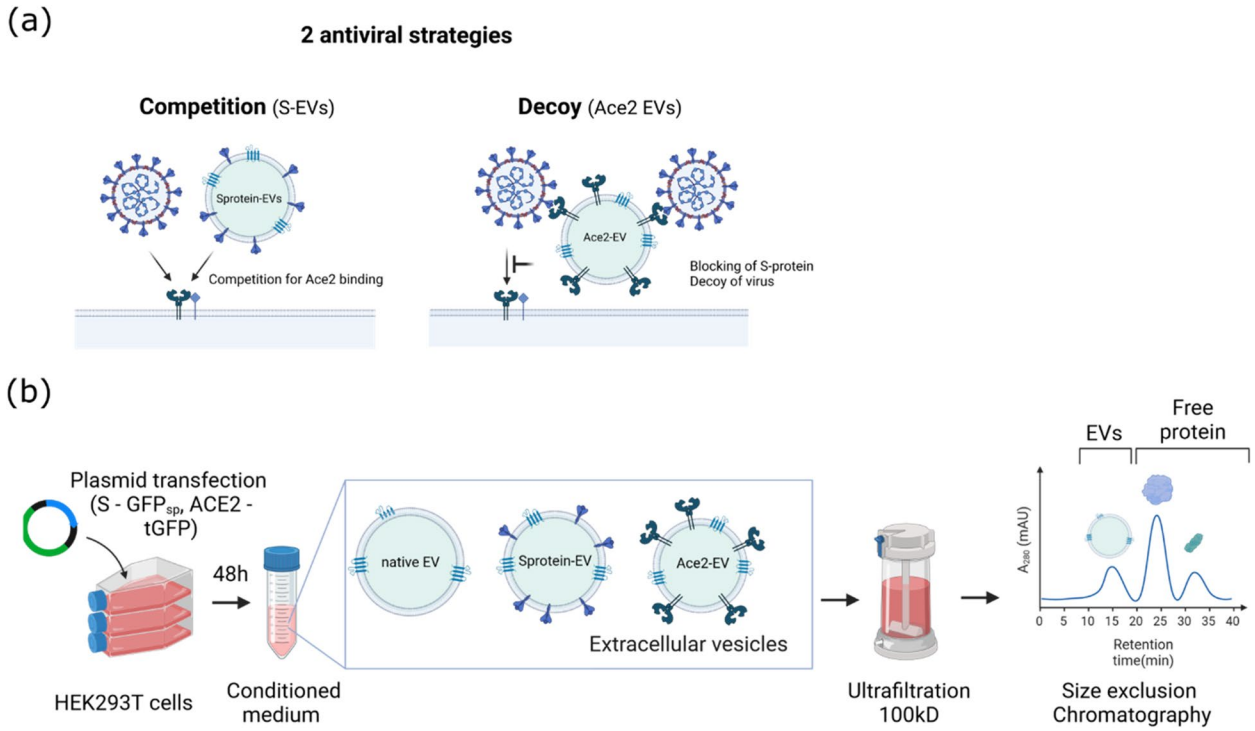

Fig. 1 Model of decoy and competition strategies and engineering of antiviral EVs. **a** Model illustrating decoy vs competition strategy of antiviral EVs. **b** General workflow for the preparation of antiviral EVs. HEK293T cells were transfected with expression constructs for either S- GFP_{sp} or ACE2 – tGFP. After 48 h, the conditioned medium (CM), containing the different EVs was collected and subjected to ultrafiltration (UF) and size exclusion chromatography (SEC) for EV enrichment

(Fig. 1b, Supplementary File 1). As revealed in previous work from our group [9] and consistent with more recent follow up studies [75], overexpression of transmembrane proteins or even EV markers does not always result in successful enrichment within extracellular vesicles and highly depends on their subcellular localisation and sorting within the producing cells. Therefore, we used GFP tagged versions of either ACE2 (ACE2 C-terminally fused to turboGFP, ACE2-tGFP) or the Spike protein of the Wuhan SARS-CoV-2 virus (Spike protein C-terminally fused to GFPspark, S-GFP_{sp}) in order to unambiguously trace and quantify their loading into EVs. CD63-mNeon was used as a control [48]. Size exclusion chromatography after UF enrichment of the conditioned medium revealed that the GFP fluorescence for all fusion proteins co-fractionated predominantly with the EV peak (Supplementary Fig. 1a). An additional smaller GFP fluorescent peak was obtained at a retention time corresponding to ca 10—50 kDa, most likely representing nonvesicular, free ACE2-GFP or S-GFP_{sp}, and/or truncated GFP protein variants. The EV peak was collected, and fractions were pooled as indicated. Interestingly, a higher GFP fluorescence was obtained in the EV peak for ACE2 as compared to the S-protein. Although two different green fluorescent proteins were used in the two constructs due to cloning reasons (turboGFP for ACE2, GFPspark for S-protein), their molecular brightnesses are relatively similar (tGFP: extinction coefficient 70,000 M-1 cm-1, quantum yield 0.53, molecular brightness 0.37; GFPsp: extinction coefficient 47,000 M-1 cm-1, quantum yield 0.60, molecular brightness 0.29; (Evrogen; SinoBiological)) thereby indicating lower engineering efficiency of S-GFP_{sp} EVs compared to ACE2-tGFP EVs. This is only partially explained by higher transfection efficiency of the ACE2-GFP transfected cells as compared to cells transfected with identical amounts of the S-GFP_{sp} expression construct (Supplementary Fig. 1a, top panels). We therefore tested the possibility to increase the sorting efficiency of S-protein into EVs by targeted mutations of the S-protein sequence. We first tested replacement of the transmembrane (Tm) and cytoplasmic domains with those of the vesicular stomatitis virus—G (VSV-G) based on an earlier study investigating the use of S-protein decorated EVs as vaccines for SARS-CoV1 [28]. As an additional strategy, we hypothesised that altering intracellular localisation of the S-protein by removal of the ERGIC targeting sequence might liberate S-protein within the cell to traffic to multivesicular bodies or the plasma membrane [31]. Of note, the addition of GFP downstream of ERGIC should already perturb its function, since KKXX

needs to be positioned at the C-terminus. However, as we did observe substantial localization of Spike-GFPsp in the perinuclear region (Fig. 2a lower left panel), we wondered whether it might nevertheless still trap some protein at the ER, thereby affecting also its sorting into extracellular vesicles. Therefore we tested whether removal of ERGIC would enhance the sorting into EVs. Constructs either replacing the Tm and cytoplasmic domains of SARS-CoV-2 with the corresponding VSV-G domains or deleting the ERGIC targeting sequence were generated from the native S-protein expression constructs by Gibson assembly and used for EV engineering following the same procedure as for the native protein.

The intracellular localisation of all GFP-tagged fusion proteins in transfected HEK293T cells was documented by fluorescence microscopy (Supplementary Fig. 2). In addition, we used co-transfection with CD63-mCherry to assess co-localisation with multivesicular bodies and the plasma membrane (Fig. 2). As expected, ACE2-GFP localised primarily to the plasma membrane with an additional fraction detected at intracellular membranes, however minimal signal in CD63-mCherry positive multivesicular bodies (MVBs) (Fig. 2a top panel and Supplementary Fig. 2). GFP-tagged native S-protein was detected primarily at the plasma membrane as well as in intracellular compartments partially co-localising with MVBs (Fig. 2a, lower left panel and Supplementary Fig. 2). Interestingly, the S-protein/VSV-G chimeric constructs largely co-localised with CD63-mCherry at both, the plasma membrane as well as within intracellular vesicles (Fig. 2a, lower middle panel and Supplementary Fig. 2). Removal of the ERGIC signal did not result in increased CD63-mCherry co-localisation and instead enhanced accumulation at perinuclear intracellular membranes (Fig. 2a, lower right panel and Supplementary Fig. 2).

Despite these differences in intracellular localisation, size exclusion chromatograms of the conditioned media collected from HEK293T cells transfected with the different S-protein variants showed no massive differences in the GFP signal co-fractionating with the EV peak except for a ca twofold reduction for the ΔERGIC construct (Fig. 2b). Consistently, quantitative single vesicle imaging using the EVAnalyzer pipeline developed in our lab [48] revealed similar fluorescence intensities of the GFP positive EVs at the single vesicle level except for the ΔERGIC S-EVs (Fig. 2c). Since neither of the mutants increased the levels of S-GFP_{sp} EVs, we focused on (GFP_{sp} tagged) native S protein for further EV characterisation and testing.

Qualitative characterisation of S-Protein and ACE2 decorated EVs

Nanoparticle Tracking Analysis (NTA) of the isolated EVs showed size distributions in the range of 110–140 nm mean size/90–120 nm mode size (Fig. 3a and Supplementary Fig. 3a). Interestingly, we observed a small but significant increase in mode size of the ACE2-tGFP engineered EVs (Fig. 3a). Similar particle/protein ratios were observed for the engineered as compared to native HEK293T EVs (Fig. 3b). Super-resolution microscopy with dSTORM imaging confirmed GFP positive clusters in a size range of ca 100–200 nm which spatially overlapped with both, CD63 as well as CD81 antibody staining (Fig. 3c). Representative images from Transmission Electron Microscopy (TEM) with negative staining are shown in Fig. 3d, confirming vesicular structures in the 100–200 nm range in all samples.

Western blotting of the EV samples confirmed the presence of canonical EV markers including the three major tetraspanins (CD63, CD81 and CD9) as well as Flotillin-1, whereas Calnexin as a negative marker was undetectable (Fig. 3e and Supplementary Fig. 3b for uncropped Western Blots). As expected, no EV markers were detected in the EV-depleted conditioned medium collected during ultrafiltration (containing mostly soluble proteins; SolF). The presence of ACE2 in the engineered EVs but none of the other EV samples was confirmed by an ACE2 antibody. Similar results were obtained for the corresponding cell lysates, which is consistent with the reported low levels or lack of ACE2 expression in HEK293T cells [42, 55]. Although we did detect TMPRSS2 to be expressed in the HEK cells used for EV production, no sorting into EVs was detected by Western Blotting. Using a commercial

(See figure on next page.)

Fig. 2 Optimisation of EV engineering for display of Spike protein and ACE2 receptor. **a** Live cell high- resolution widefield fluorescence microscopy (100 × oil objective, NA1.45) of HEK293T cells after co- transfection of the different constructs with CD63-mCherry. Lower panel left: GFP_{sp} tagged Spike protein of the Wuhan SARS-CoV-2 variant (S—GFP_{sp}); Lower panel middle : S—GFP_{sp} with replacement of the transmembrane (TM) domain by the TM domain of VSV –G; Lower panel right : S—GFP_{sp} with elimination of the Endoplasmic Reticulum Golgi-Intermediate Compartment localization domain (S(Δ ERGIC)-GFP_{sp}). Top panel: ACE2 tagged with turboGFP (ACE2-tGFP). Single transfection of the respective plasmids are shown in Supplementary Fig. 1. Scale bars: 2 µm or 5 µm as indicated. **b** Analytical SEC of CMs harvested from HEK293T cells with and without transfection with the different constructs as indicated. Chromatograms are shown for detection of the GFP fluorescence measured at 488 nm/510 nm (ex./em.). Zoom-in shows the EV peak eluting at a retention time of ca. 10 min. **c** Single vesicle imaging performed on CMs collected from HEK293T cells transfected with different S—GFP_{sp} plasmids. Mean ∑ intensity/particle represents the total fluorescence detected per particle and was calculated as area x mean pixel intensity per spot. Data represent replicates with means and standard deviations of 10 individual fields of view per sample

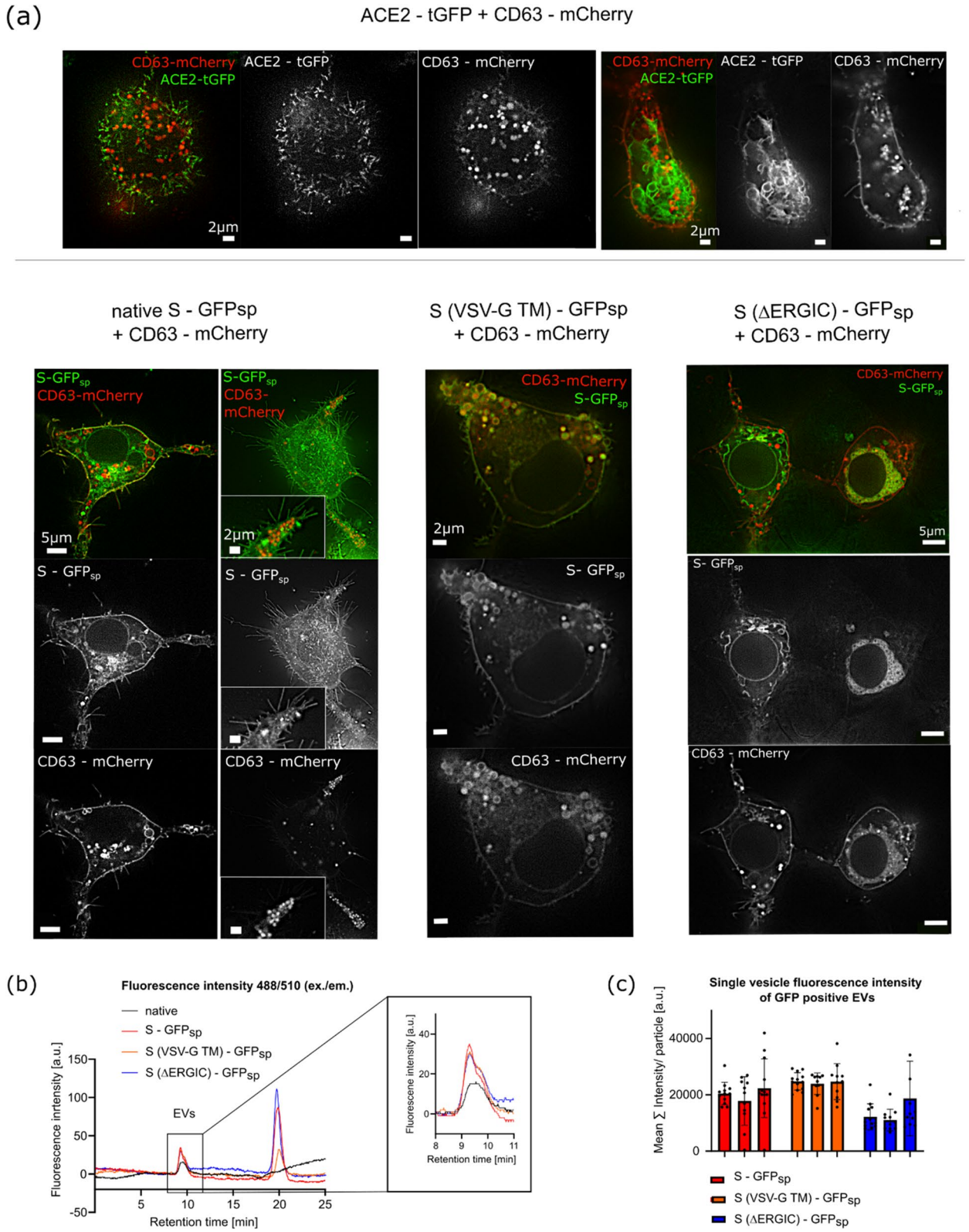

Fig. 2 (See legend on previous page.)

antibody raised early in the pandemic against the SARS-CoV-2 Spike protein (ab272504; abcam), we confirmed the specific expression of the S-GFP$_{sp}$ fusion protein in lysates from cells with the corresponding construct. However, no signal was detected in the EVs recovered from these cells. This is likely due to a low abundancy of S-GFP$_{sp}$ modified EVs, as indicated by the low GFP fluorescence in the EV peak detected by analytical SEC (Supplementary Fig. 1a). Testing the Abcam anti-S antibody for immunostaining also failed to detect the protein on intact EVs by single vesicle imaging (data not shown).

In the course of this study, several additional anti-S antibodies became available, one of them was also successfully detected S-GFP$_{sp}$ in cell lysates and recombinant S-protein positive controls by Western Blotting (Fig. 3f and Supplementary Fig. 3c for uncropped Western Blot). As shown in Fig. 3g, using this antibody (GTX632604-100; GeneTex) for immunostaining and quantitative single vesicle imaging confirmed the presence of Spike protein in at least 80% of the GFP positive EVs. An additional fraction of S-positive EVs was detected which did not show any GFP signal (Supplementary Fig. 3d). Since only a small fraction of unspecific, false positive spots was detected in native HEK293T EVs under identical conditions (Supplementary Fig. 3d; right panel), this can most likely be explained by a fraction of processed S-protein lacking the GFP tag, and/or different detection thresholds for 1:1 GFP-tagged proteins (detection limit on our widefield microscope in the range of 3–5 molecules of GFP per EV) as compared to multiply labelled secondary antibodies [48].

Since endogenous antibodies raised during an infection are specifically directed against intact Spike protein exposed on cellular and virus membranes, we additionally tested the recognition of S-GFP$_{sp}$ positive EVs by sera from a voluntary donor recovered from infection with SARS-CoV-2 during the first wave of the pandemic in Austria. A serum pool containing serum from 50 healthy, unvaccinated voluntary blood donors was used as negative control. The infection status of all donors was monitored using an anti-N electrochemiluminiscence immunoassay (ECLIA) (Supplementary Table 1a). In addition, the presence of specific SARS-CoV-2 antibodies in the serum of the three COVID-19 convalescent plasma donors was confirmed by an anti-N ECLIA (Supplementary Table 1c). Antibody functionality was confirmed by an ELISA-based surrogate virus neutralisation test (Supplementary Table 1c). One donor was then selected for testing reactivity of virus antibodies with S-GFP$_{sp}$ engineered EVs (Fig. 3h-i). Western Blotting using recombinant S-protein confirmed again the presence of anti-Spike antibodies (Fig. 3h and Supplementary Fig. 3c for uncropped Western Blots). After incubation of S-GFP$_{sp}$ EVs with either the serum from the COVID-19

(See figure on next page.)

Fig. 3 Qualitative characterisation of S-protein and ACE2 decorated EVs. **a** Size distribution of UF-SEC purified native HEK293T EVs as compared to EVs from S-GFP$_{sp}$ or ACE2-tGFP transfected HEK293T cells as measured by NTA. Box plots are shown for mean and mode sizes from 6 biological replicates and 15 technical replicates each with 5–95% confidence intervals (CI). A significant increase (*, p = 0.018) in the mode size is observed for ACE2- tGFP as compared to native HEK293T EVs. Statistics: Ordinary one-way ANOVA. **b** Particles per mg protein ratios for the different engineered and native HEK293T EVs, as assessed by normalizing particle concentrations determined by NTA to protein concentrations determined by Bradford. Data represent averages with standard deviations of 6 independent EV preparations each. Statistics: One-way ANOVA. **c** Representative direct Stochastic optical reconstruction microscopy (dSTORM) images of S-GFP$_{sp}$ (upper panel) or ACE2-tGFP (bottom panel) EVs stained with Alexa Fluor 555 labelled anti-CD63 or anti-CD81 antibody (Oxford Nanoimager). Every dot represents one individual blinking event derived either from individual fluorophores or repeated blinking of the same fluorophore. Scale bars: 100 nm or 200 nm as indicated. **d** Representative TEM images with negative staining of native EVs, S-GFP$_{sp}$ EVs, and ACE2-tGFP EVs. Scale bars: 50 nm. **e** Western Blot analysis of UF-SEC purified EVs, EV-depleted conditioned medium (soluble fraction, SolF) and cell lysates of native, S-GFP$_{sp}$ and ACE-tGFP transfected HEK293T cells with detection for different tetraspanins (CD9, CD81 and CD63), Flotilin-1, Calnexin, TMPRSS2, ACE2 or S-Protein as indicated. **f** Western Blot of cell lysates derived from native and S-GFP$_{sp}$ transfected HEK293T cells and on recombinant SARS-CoV2 Spike protein with an anti-S-Protein antibody (GeneTex). **g** Single vesicle imaging of UF-SEC purified EVs from S-GFP$_{sp}$ transfected HEK293T cells using the same anti-S antibody (GeneTex) as in (f). Representative images (left panel) of samples incubated with primary and secondary antibody are shown. Samples incubated with secondary antibody only were used as negative controls. Particles detected by the antibody are pseudo-coloured in red, S-GFP$_{sp}$ EVs are shown in green and co-localisation in yellow. Data for native HEK293T EVs are shown in Supplementary Fig. 3 d. Scale bars: 2 µm. Framed areas represent zoom ins. Mean % of co-localisation of S-GFP$_{sp}$ positive particles detected by the antibody (red in green coloc) and % of total particles recognized by the antibody colocalising with a detectable S- GFP$_{sp}$ (green in red coloc) was calculated from 10 individual fields of view. **h** Western Blot of recombinant SARS-CoV-2 Spike protein (200 ng or 500 ng) incubated with sera from SARS-CoV-2 positive or negative donors used as primary antibody. HRP-labelled goat-anti-human (IgG) was used as secondary antibody. **i** Single vesicle imaging of EVs isolated from S-GFP$_{sp}$ transfected HEK293T cells after immunofluorescence detection, using sera from SARS-CoV-2 positive or negative donors as primary antibody and Alexa Fluor 555 labelled goat-anti human(IgG) as secondary antibody. Representative high-resolution widefield fluorescence microscopy images (100 × NA 1.45 oil immersion objective) are shown in the middle panel. Particles detected by the serum-derived antibodies are pseudo coloured in red, S-GFP$_{sp}$ EVs are shown in green and co-localisation in yellow. Scale bars: 2 µm. Framed areas represent zoom ins. Mean % of co-localisation of S-GFP$_{sp}$ recognised by the sera (red in green coloc) and % of total sera- recognized particles colocalising with a S-GFP$_{sp}$ (green in red coloc) was calculated from 10 individual fields of view. Samples incubated with the secondary antibody only were used as negative controls

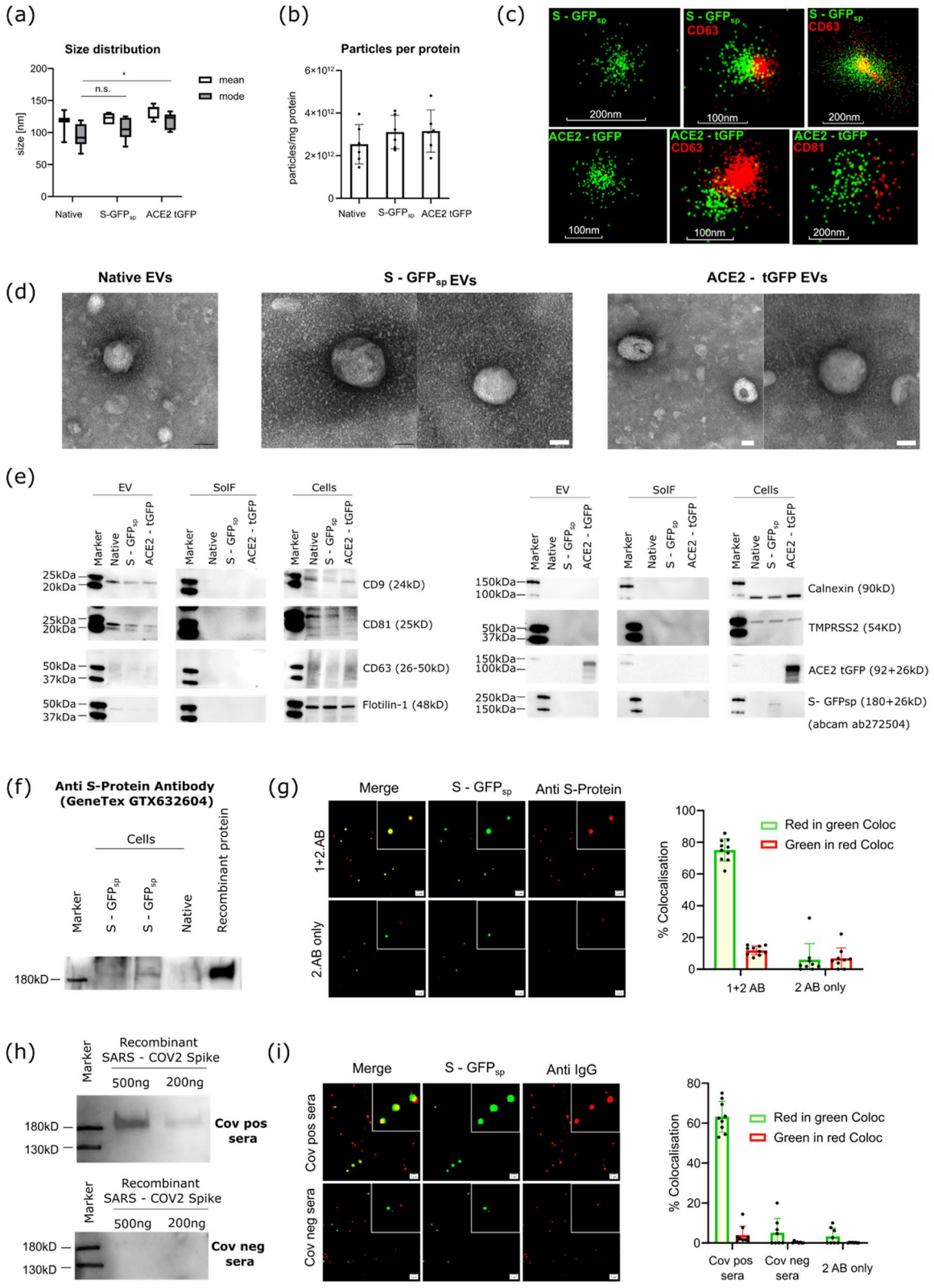

Fig. 3 (See legend on previous page.)

positive donor or the serum pool from uninfected and unvaccinated donors we performed single vesicle imaging with anti-IgG detection (Fig. 3i). This confirmed that, the serum from the COVID-19 positive donor contained IgG antibodies recognising at least 60% of all S-GFP$_{sp}$ EVs, which was not the case for the healthy donor serum (Fig. 3i). The total number of EVs detected under all conditions are shown in Supplementary Fig. 3e, indicating a relatively large additional fraction of HEK293T EVs non-specifically detected by the anti-human secondary antibody but not co-localising with S-GFP$_{sp}$.

Together these data directly demonstrate both the presence, and surface exposure of S-protein on the engineered EVs, and its accessibility to ligands even in the protein rich environment of serum, thereby ruling out shielding by a possible protein corona being formed.

Quantitative single vesicle characterisation of engineered ACE2-GFP and S-GFP$_{sp}$ HEK293T EVs

Several studies have been reported by now which explored EVs decorated with ACE2 as antivirals [70] or S-protein from SARS-CoV-1 or SARS-CoV-2 for vaccination [26, 46]. However, only minimal information is currently available on the origin and types of extracellular vesicles underlying these populations, as well as their quantitative contribution to the overall vesicle numbers within the samples. We therefore further characterised the engineered EVs by immunostaining for the three major tetraspanin EV markers CD63, CD81 and CD9 (Fig. 4a and Supplementary Fig. 4a). EVs from cells transiently transfected with CD9-emGFP, CD81-emGFP as well as a HEK293T line stably overexpressing CD63-mNeon were used as positive controls for antibody validation. Alternatively, we generically labelled all protein-containing vesicles and nanoparticles in the samples using Cy5-NHS chemistry to assess the relative fraction of engineered EVs over all particles (Fig. 4b and Supplementary Fig. 4b). Samples were analysed by single vesicle imaging and quantified using EVAnalyzer [48].

As shown in Fig. 4a (right panel) (% co-localisation red in green), both S-GFP$_{sp}$ as well as ACE2-tGFP EVs were predominantly positive for CD9 (ca 50% and 40%, respectively) and CD81 (ca 60% and 55%, respectively) which, in contrast to CD63, are known to primarily localize to the plasma membrane rather than to multivesicular bodies [17]. Only a small fraction of the GFP-positive EVs in both samples were positive for CD63 (ca 30% and 25%, respectively). This is consistent with the localisation of the corresponding fusion proteins in the parent cells (Supplementary Fig. 2) and indicates that these vesicles primarily derive from the plasma membrane with a smaller contribution from multivesicular bodies. Conversely, ACE2-tGFP or S-GFP$_{sp}$ EVs (green) constitute only a relatively small fraction of all tetraspanin positive EVs (red), as revealed by the converse analysis of percentage co-localisation of green in red. Similarly, also generic detection of all particles by Cy5-NHS indicated that only a minor fraction of all detected particles is positive for the GFP-fusion proteins (Fig. 4b). Both analyses confirmed again that ACE2-tGFP overexpression generally resulted in a ca 3- to 5-fold higher number of engineered EVs as compared to engineering with S-GFP$_{sp}$. The relative difference between the two types of engineered EVs is consistent with data generated by Nano-Flow-Cytometry (nano-FCM). The absolute numbers of GFP positive overall EVs, however is generally higher for all samples (Supplementary Fig. 4c) as compared to single vesicle imaging, which is likely due to the scatter based detection threshold and thus lower sensitivity for the total EV population in Flow-Cytometry.

Interestingly, EVs from ACE2-GFP transfected cells resulted in ca 2- to 3-fold higher Cy5-NHS labelling efficiency as revealed by both, analytical SEC with simultaneous GFP/Cy5 fluorescence and UV280 nm detection (Supplementary Fig. 4b) and single vesicle brightness

(See figure on next page.)

Fig. 4 Quantitative characterisation of engineered EV subpopulations by single vesicle imaging. **a** EVs isolated from native, S-GFP$_{sp}$ or ACE2-tGFP transfected HEK293T cells were immunostained with antibodies targeting either of the three tetraspanins CD9, CD63 and CD81 with detection by an Alexa Fluor 555 labelled secondary antibody. EVs from HEK293T cells transiently transfected with CD9-emGFP or CD81-emGFP or stably expressing CD63-mNeon were used as a positive control for each of the antibodies. Representative high-resolution widefield fluorescence microscopy images (100 × NA 1.45 oil immersion objective) for each tetraspanin are shown in the left panel. Particles detected by the antibody are pseudo coloured in red, fluorescent protein (FP)–tagged EVs (GFP, tGFP, GFP$_{sp}$ or mNeon) are shown in green and co-localisation in yellow. Scale bars: 1 µm. The % co-localisation was calculated from 10 individual fields of view and is shown in the right panels. Red in green: % of tetraspanin-FP, S-GFP$_{sp}$ and ACE2-tGFP co-localising with the respective tetraspanins. Green in red: % of immune-positive particles co-localising with a genetically engineered tetraspanin, S-GFP$_{sp}$ or ACE2-tGFP. Statistics: t-test. **b** Native, CD63-mNeon, S-GFP$_{sp}$ or ACE2-tGFP HEK293T EVs were covalently labelled with CY5-NHS with removal of free dye by size exclusion chromatography (Supplementary Fig. 4b). Representative images are shown in the left panel. The percentage of FP- (GFPsp, tGFP, mNeon) positive spots per CY5-NHS labelled particles as well as the single vesicles fluorescence intensity of Cy5 are shown in the right panels. Means and standard deviations are calculated from 10 individual fields of view. Statistics: One-way Anova. **c** Single vesicle fluorescence intensity of ACE2-tGFP, S-GFP$_{sp}$ or CD63 mNeon HEK293T EVs. Data represent mean sum intensity per spot (calculated as area * average intensity) for three independent samples with averages and standard deviations from 10 individual fields of view

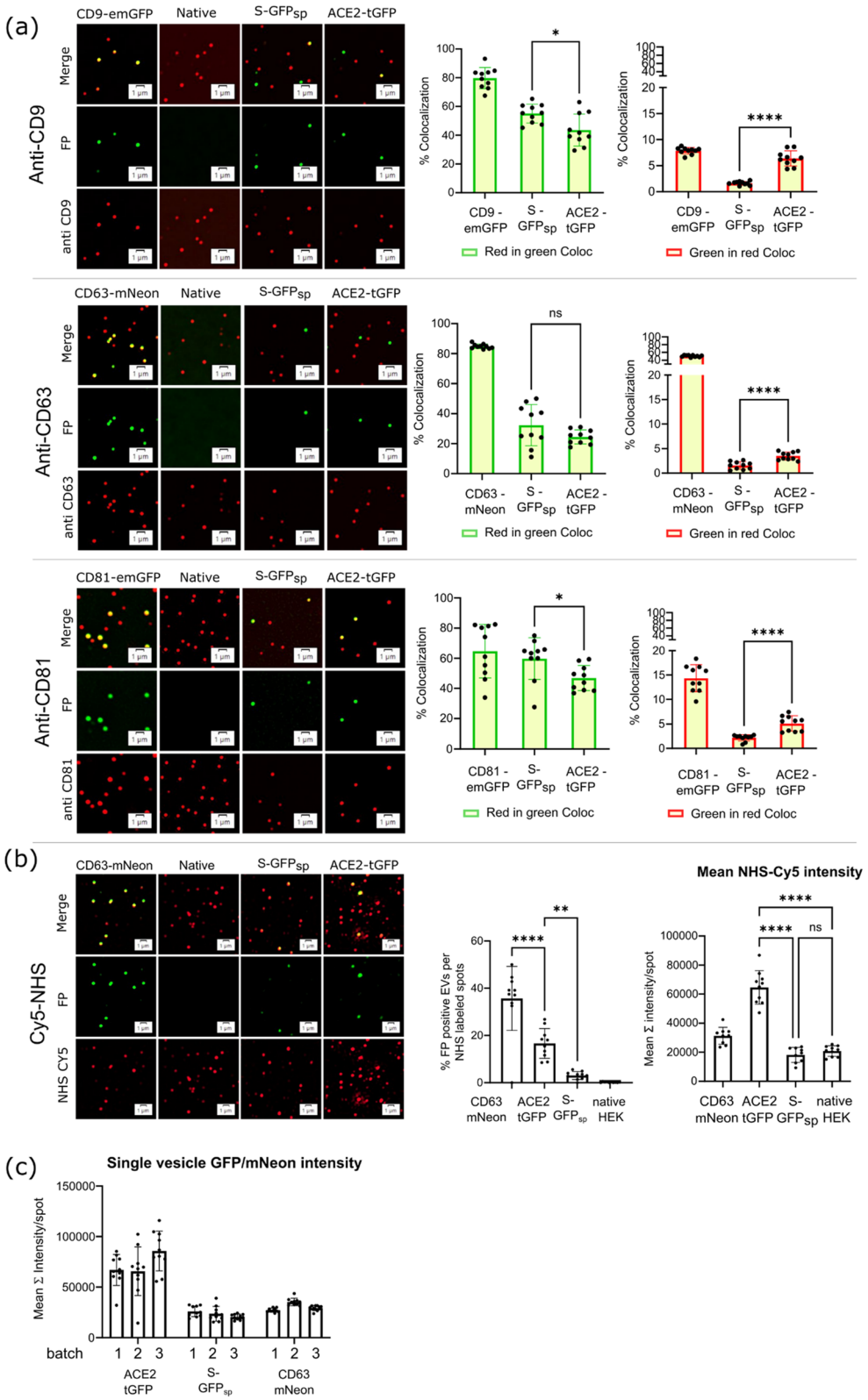

Fig. 4 (See legend on previous page.)

analysis from the imaging analysis (Fig. 4b, right panel). This is consistent with the slightly increased size of these vesicles detected by NTA (Fig. 3a) and suggests that ACE2 engineering results in increased availability of protein-derived primary amines on the EV surface. Further, the single vesicle brightness in the GFP channel was ca 3-fold higher for ACE2-tGFP than for S-GFP$_{sp}$ as well as CD63-mNeon EVs (Fig. 4c), suggesting that the average stoichiometry of ACE2 on the engineered EVs is higher than for the other two proteins.

Spike protein and ACE2 decorated EVs maintain cell uptake activity in Vero cells

The basic physicochemical characterisation of the engineered EVs did not indicate any global changes in morphology or concentrations of the vesicles with an only slightly increased size for the ACE2 EV. However, it is worthwhile to note, that due to the small percentage within the whole population the individual engineered vesicles might be affected to a larger extent than can be detected by bulk measurements. It is therefore conceivable that these two large proteins on the surface might nevertheless interfere with the biological activity of the EVs. Since cell uptake is one of the key functions of extracellular vesicles, we therefore tested whether ACE2-tGFP and S-GFP$_{sp}$ decorated EVs are still internalised by recipient cells. Vero cells were used as they are a relevant model for SARS virus replication [43]. Cells were grown in optical bottom 96-well plates and incubated with S-GFP$_{sp}$ or ACE2-tGFP EVs at increasing concentrations for 3 h. Internalised EVs were detected after stringent washing and cell fixation using automated high resolution widefield scanning microscopy and quantified after image deconvolution by EVAnalyzer [48]. Both types of GFP positive EVs were still recognised and taken up by the Vero cells and show the typical perinuclear accumulation of light diffraction limited, individual spots (Fig. 5a, left panels), previously well described as a hallmark of EV cell uptake [21]. The average number of S-GFP$_{sp}$ internalised EVs per cell was generally lower than for ACE2-tGFP EVs (Fig. 5a, right panels) when doses are matched based on total particle concentrations (determined by NTA) (Fig. 5a; black axis). Comparison of doses matched by molarities of fluorescent particles (as calculated from Fig. 4b) on the other hand show an IC$_{50}$ in the same range for ACE2- EVs as compared to S-EVs. The number of total particles detected in the cells at saturation was lower for S-GFP$_{sp}$ EVs (Fig. 4c) than ACE2-tGFP EVs, most likely due to their lower brightness resulting in a lower detection efficiency over the relatively high cellular autofluorescence in the GFP channel. To simultaneously monitor uptake of the S-GFP$_{sp}$ EV subpopulation over all CD63 positive EVs, we used EVs from cells double transfected with either CD63-mCherry and S-GFP$_{sp}$ (Fig. 5b) or with CD63-mCherry and ACE2-tGFP (Fig. 5c). No apparent difference was observed in the localisation of internalised CD63-mCherry EVs with and without the S-GFP$_{sp}$ or ACE2 protein (Fig. 5b, upper panel). The number of CD63-mCherry as compared to the S-GFP$_{sp}$ EVs per cell was ca 10-fold higher (Fig. 5b, left panel). This is highly consistent with the ca 10-fold higher number of CD63-mCherry as compared to S-GFP$_{sp}$ EVs in the sample (Fig. 5b). This was similar for ACE2-tGFP EVs. In addition, the co-localisation of S-GFP$_{sp}$ and CD63-mCherry and co-localisation of ACE2-tGFP and CD63 mCherry both in vitro and after cell uptake in situ was comparable (Supplementary Fig. 5a and b). Therefore, we conclude that the S-GFP$_{sp}$ engineered EVs and ACE2-tGFP engineered EVs are internalised with comparable efficiency and result in similar subcellular localisation as CD63 positive EVs in these recipient cells.

Antiviral activity of ACE2-tGFP EVs and S-EVs in a pseudovirus assay

The ability of ACE2-tGFP EVs (Fig. 6a) and S-GFP$_{sp}$ EVs (Fig. 6b) to either decoy or compete with SARS-CoV2 cell entry was tested in a pseudovirus (PV) assay in Chinese hamster ovarian (CHO) cells. To test dependence on the canonical ACE2/TMPRSS2 pathway we used both, CHO cells with stable lentiviral overexpression of ACE2 and TMPRSS2 (CHO ACE2 +/T2 +), as well as wild type cells which are negative for both, ACE2 and TMPRSS2 (CHO ACE2-/T2- cells). Native HEK293T EVs (Supplementary Fig. 6), as well as a vesicle depleted fraction collected after UF (soluble fraction, SolF) were used as controls for nonspecific activity of non-engineered EVs

(See figure on next page.)

Fig. 5 Functional characterisation of the EVs. **a** Uptake of S – GFP$_{sp}$ EVs or ACE2 – tGFP EVs (**a**) or EVs derived from double transfected S-GFP$_{sp}$/CD63 mCherry or ACE2-tGFP/CD63 mCherry cells (**b** and **c**) into Vero cells. Cells were seeded in a 96 well plate and incubated with different EV concentrations for 3 h. After fixation, cells were stained with Hoechst33342 and imaged by automated scanning widefield fluorescence microscopy. The dose response of EV uptake quantified by the number of fluorescent spots per cell as determined by the Fiji plugin EVAnalyzer [48] is shown in the right panel. Data represent averages from 15 images per well and three replicate wells each. EV concentrations at half-maximal saturation (EC$_{50}$) were determined by nonlinear curve fitting. Vesicle concentrations are additionally specified as ACE2-tGFP and S-GFP$_{sp}$ positive molarities, as calculated by correction of total molarities using the experimentally determined % of engineered EVs depicted in Fig. 4a (blue/top x-axis). Representative images at different concentrations as indicated are shown in the left panels. Scale bars: 20 µm or 2 µm for the zoom ins (a) and 10 µm (b)

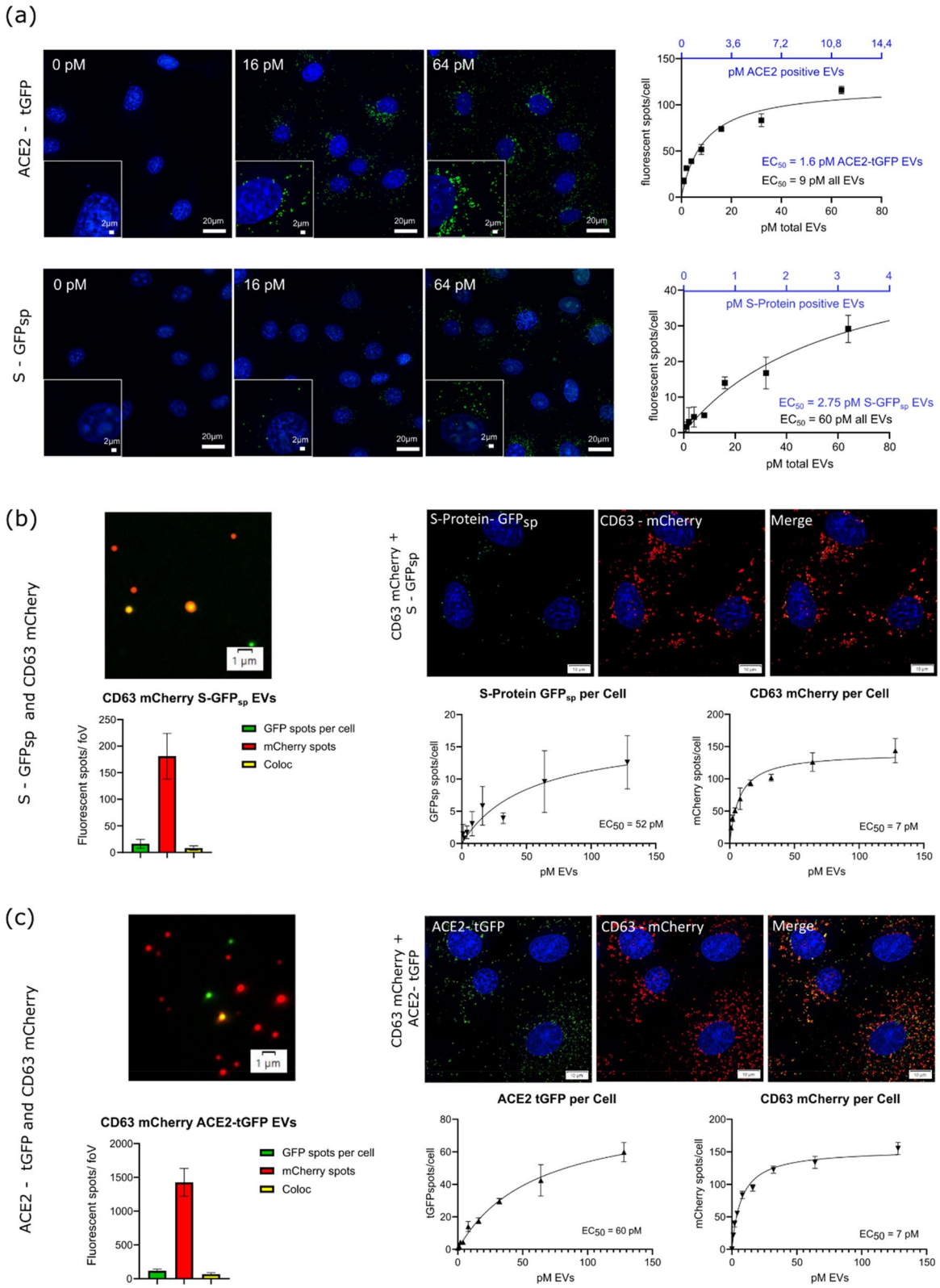

Fig. 5 (See legend on previous page.)

or secreted non-vesicular components. In addition, we used widely established neutralising antibodies against either ACE2 or Spike protein (Fig. 6c) as well as WHO standard patient sera (Supplementary Fig. 6b) to benchmark the potency of the antiviral EVs quantitatively.

Pseudovirus was generated in HEK293T/17 cells [13] by transfection with three different vectors containing a lentiviral packaging construct, a firefly luciferase reporter construct, as well as either of the different SARS-COV Spike protein variants. To cover the major viral clades, we tested the Spike protein variants of D614G, the first variant that emerged in Italy in February 2020, BA.1Omicron as the last emerging variant at the time of this study as well as the SARS-CoV-1 Spike protein. Levels of PV uptake were measured as relative light units (RLU) of luciferase within the cells after 48 h of cell/virus co-incubation with the virus. RLUs with and without virus are indicated in grey (± SD). As expected, in ACE2/TMPRSS2 expressing cells, the addition of all pseudovirus variants resulted in a > 1000-fold increase in RLUs (Fig. 6a and b and Supplementary Fig. 6a; upper panels). Consistent with the previously demonstrated general dependence of all SARS-CoV-2 variants on ACE2 receptor binding, no significant luciferase reporter signal was obtained after pseudovirus addition to ACE2-/T2- cells (Fig. 6a and b and Supplementary Fig. 6a lower panels). PV infection was inhibited in a dose dependent manner by neutralising antibodies (Fig. 6c). The ACE2 mAb showed comparable inhibitory potency against all 3 tested SARS-CoV PV variants with highly similar IC50ies ranging from 0.11- 0.17 µg/mL of added antibody. In contrast, neutralisation with the S-protein antibody resulted in ca 40-fold lower potency for Omicron as compared to D614G or SARS-CoV-1 PV, consistent with an altered antibody binding efficiency to different Spike variants.

Antiviral activity of the engineered EVs was tested by co-incubation of the pseudovirus in presence of the EVs at different concentrations ranging from 1×10^8 to 1×10^{11} particles per mL as determined by NTA. ACE2-tGFP EVs showed a strong, concentration-dependent inhibition of PV uptake (Fig. 6a) for all tested variants (SARS-COV-2: D614G BA.1 Omicron; and SARS-COV-1) with IC_{50}ies in the range of 2×10^9—2×10^{10} particles per mL. Using the single vesicle data in Fig. 4b, we corrected these numbers for the fraction of engineered EVs over all particles (as detected based on Cy5-NHS labelling) and converted them additionally into molar concentrations, resulting in IC_{50}ies ranging from 0.7 pM to 4.7 pM of ACE2-tGFP positive EVs (Table 2). In contrast, no inhibition of the pseudovirus was observed for Spike-protein decorated EVs, which even resulted in a small but significant increase of luciferase reporter signal for all tested variants (Fig. 6b). This is not due to a photophysical artefact of GFP fluorescence contributing to the luminescence, since control experiments with addition of S-GFP_{sp} EVs without any pseudovirus did not result in an increased luciferase signal (Supplementary Fig. 6c). An alternative explanation might be that binding of the Spike protein to ACE2 receptors might induce secondary effects in the cells, priming them for enhanced PV uptake. We therefore additionally tested pseudovirus infection after pre-treatment of the cells with S-GFP_{sp} EVs for 1 h and removal of the EVs prior to pseudovirus addition, rather than co-incubation. Under these conditions, we observed no increase in luciferase reporter signal (Supplementary Fig. 6d). Together this indicates that S-GFP_{sp} EVs directly enhance, rather than inhibit SARS-CoV-2 pseudovirus uptake in this reporter assay system. No effect was detected for native HEK293T EVs as well as EV-depleted matched samples for all constructs.

Together, these data revealed that engineered decoy (ACE2-) EVs are between 1000–40000-fold more potent in SARS-CoV cell entry inhibition when comparing molarities of vesicles with molarities of free antibody (Table 2). This high potency as compared to free antibody, is likely explained by an increased avidity due to multiple ACE2 receptors per particle, which can therefore bind multiple viruses at the same time.

(See figure on next page.)

Fig. 6 Antiviral activity of EVs tested with the pseudovirus (PV) assay. Assay performed on CHO ACE2 +/T2 + cells or on CHO ACE2 -/T2- cells using PV engineered to display different Spike protein mutants (SARS-COV-2: D614G, BA.1 Omicron; SARS-COV-1). Cells were treated with native EVs (Supplementary material; grey), Spike EVs **(b; blue)** or ACE2-EVs **(a; red)** or their corresponding EV depleted conditioned media (bright red, blue and grey). Cells without PV treatment (no virus) or with PV treatment alone (+ virus) ± SD are indicated in grey. Mean RLU of > 3 independent measurements are shown for different EV concentrations at constant PV concentrations. IC_{50} is determined by sigmoidal curve fitting with bottom and top constrained for values obtained by cells with and without virus controls. **(c)** CHO ACE2 +/T2 + cells, treated with PVs engineered to display different Spike protein mutants (D614G, BA.1 Omicron SARS 2, SARS1 COV1) with and without an ACE2 monoclonal antibody #105 and a S-Protein Receptor binding domain (RBD) monoclonal antibody. The antibody was used at different concentrations as indicated and IC_{50} is determined by sigmoidal curve fitting with bottom and top constrained for values obtained by cells with and without virus controls

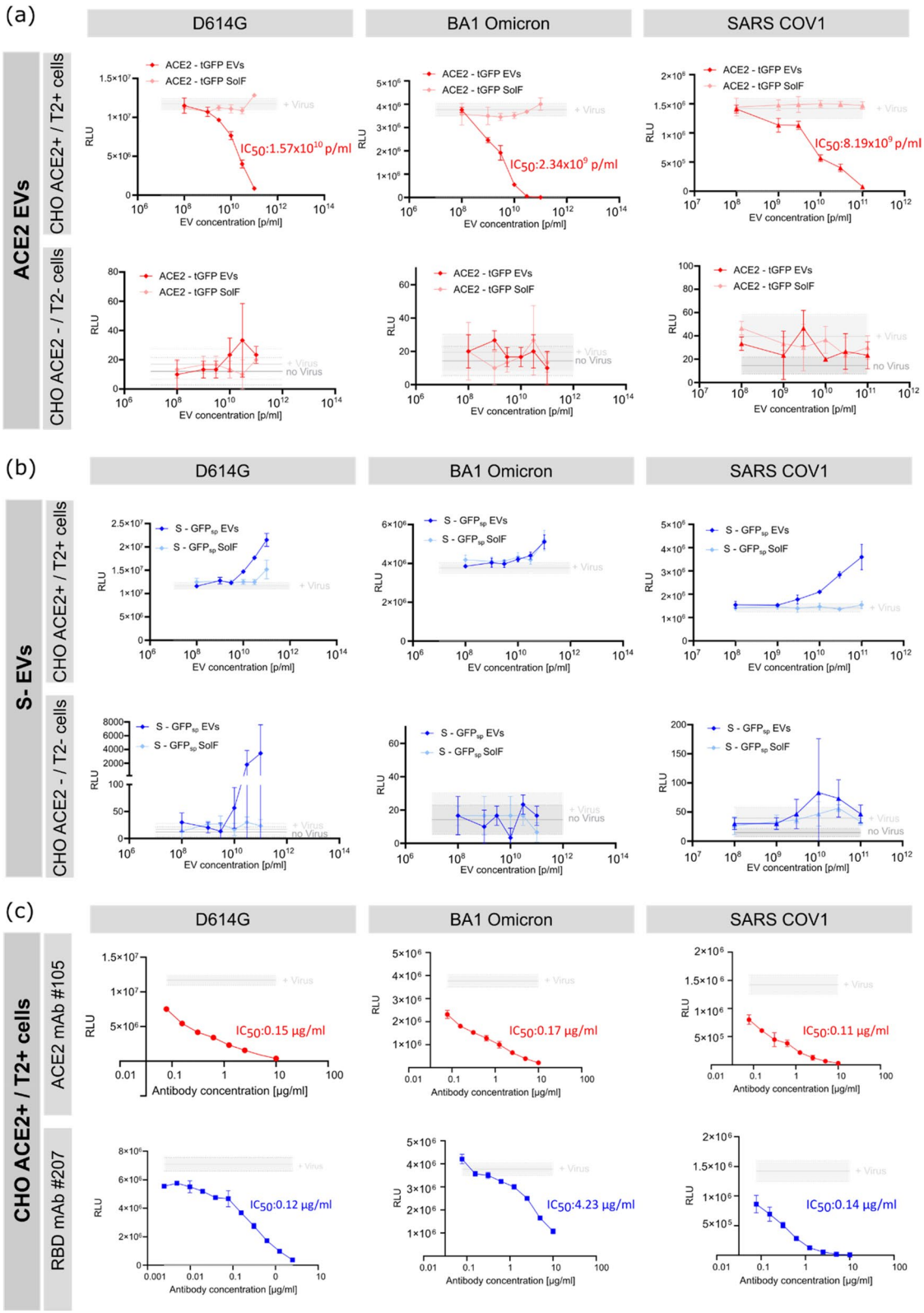

Fig. 6 (See legend on previous page.)

Table 2 Comparison of all IC_{50} values determined from PV experiments illustrated in Figure 6 with normalized EV concentration

%		D614G				BA1 Omicron				SARS COV1			
		IC50 [p/ml] or [µg/mL]	IC50 [pM]	ACE2 positive particles [%]	IC50 corrected [pM]	IC50 [p/ml] or [µg/mL]	IC50 [pM]	ACE2 positive particles [%]	IC50 corrected [pM]	IC50 [p/ml] or [µg/mL]	IC50 [pM]	ACE2 positive particles [%]	IC50 corrected [pM]
EVs	ACE2 - tGFP Evs	1.57 ± 0.3E+10	26,07	18	4,69	2,34E+09	3,762058	18	0,68	8,19E+09	13,6	18	2,45
	S- GFP_{sp} Evs	n.a.		5	n.a.	n.a.		5	n.a.	n.a.		5	n.a.
ANTIBODIES	ACE2 antibody	0,15	1014	-	1014	0,17	1100	-	1100	0,11	747	-	747
	Spike RBD antibody	0,12	780	-	780	4,23	28210	-	28210	0,14	947	-	947

Inhibition of viral replication by engineered EVs in infection models with native SARS-CoV-2 virus

Given that pseudovirus assays predominantly model the cell entry step and not the entire viral replication cycle or cellular responses to the infection, we next tested the potential of engineered EVs to inhibit SARS-CoV-2 replication using a plaque assay. Vero cells were infected using a total of 50pfu per wellof the native SARS-CoV-2 D614G virus in the presence or absence of engineered or native EVs at two different concentrations. One-hour post-infection, the medium was replaced and, cells were overlaid with methylcellulose to allow plaque formation directly in transfected Vero cells. Consistent with the pseudovirus data, a dose dependent reduction of plaque formation was observed when the virus was incubated with ACE2-EVs (Fig. 7a middle panel). In contrast, native HEK293T EVs and the EV-depleted soluble fraction (Fig. 7a white bars and left panel) did not affect viral replication. Interestingly, unlike in the pseudovirus assay, the S-GFP_{sp} engineered vesicles also significantly inhibited replication of the native virus (Fig. 7a, right panel).

To test the antiviral effects over time, Calu-3 cells were infected with the SARS-CoV-2 D614G variant in the presence or absence of the different EVs for 1 h. The kinetics of viral replication was then determined by measuring viral titres in the supernatant harvested every 24 h up to 6 days post- infection via plaque titration in Vero cells. As shown in Fig. 7b, treatment with the ACE2-tGFP EV reduced viral titres by approximately two orders of magnitude (log_{10}) at 24 h post-infection, with this reduction maintained throughout the culture duration. S-GFP_{sp} EVs also effectively inhibited viral replication in Calu-3 cells, albeit again with lower efficiency than ACE2-tGFP EVs. As in the other models, the EV depleted soluble fraction again did not show any effect on viral load (Supplementary Fig. 7a).

To validate the efficacy under conditions closer to the physiological context, a 3D-model incorporating primary human bronchial epithelial cells (HBEC) and human nasal epithelial cells (HNEC) was employed to assess the inhibitory effects of the engineered EVs on SARS-CoV-2 replication (Fig. 7c). As shown in Fig. 7d, SARS-CoV-2 production after infection via the epithelial apical surface increased sharply, from 4.5 log_{10} PFU/ml at 24 h to 7.5 log_{10} PFU/ml at 72 h post-infection. Treatment of HBEC with the virus in the presence of ACE2-tGFP EVs decreased viral production approximately 100 fold to 2.5 log_{10} PFU/ml after initial 24 h post-infection at the dose of 10^{11}/ml EVs, whereas S-GFP_{sp} EV treatment at matched concentrations reduced the viral titres to approximately 4 log_{10} PFU/ml at 24 h post-infection. Similar results were obtained for the nasal epithelial model (HNEC, Fig. 7d, right panel). Again, no effect was observed upon addition of EV depleted conditioned medium (SolF; Supplementary Fig. 7b). Interestingly, while the engineered EVs showed a strong reduction of viral numbers at onset (~ 100 fold) for all 3 tested models (Fig. 7b,d), the viral replication progressed delayed but at similar slope in the Calu3 and Nasal epithelium. This is consistent with an inhibition of the initial infection and indicates that there is no relevant contribution of secondary cellular responses to the engineered EVs in these models. Interestingly, in the bronchial epithelium model, viral replication is further slowed down throughout the monitoring time post infection together with ACE2 EVs, despite both viral and vesicles have been removed after the one-hour infection (Fig. 7d, left panel). A therapeutic effect will therefore be most effective at initial stage of infection, when viral loads are still low or can be achieved through repeated dosing, as compared to viral particles, EVs do not replicate and are therefore not able to outcompete high viral loads over time.

These results were confirmed by immunofluorescence analysis of the HBEC stained with anti-nucleocapsid and anti-Spike Abs (Fig. 8). The antiviral stainings were prominently detectable both in HBECs treated solely with the virus and those co-treated with native EVs (Fig. 8, upper panels). Notably, infected cultures treated with ACE2-tGFP EVs exhibited no nucleocapsid and Spike antigens, suggesting an inhibition at the level of viral entry. Consistent with results from the plaque forming assay, treatment with S-GFP_{sp} EVs also reduced viral antigen detection albeit at lesser extent compared to ACE2-tGFP EVs, as illustrated by the presence of a limited number of virus positive cells which were however well below the

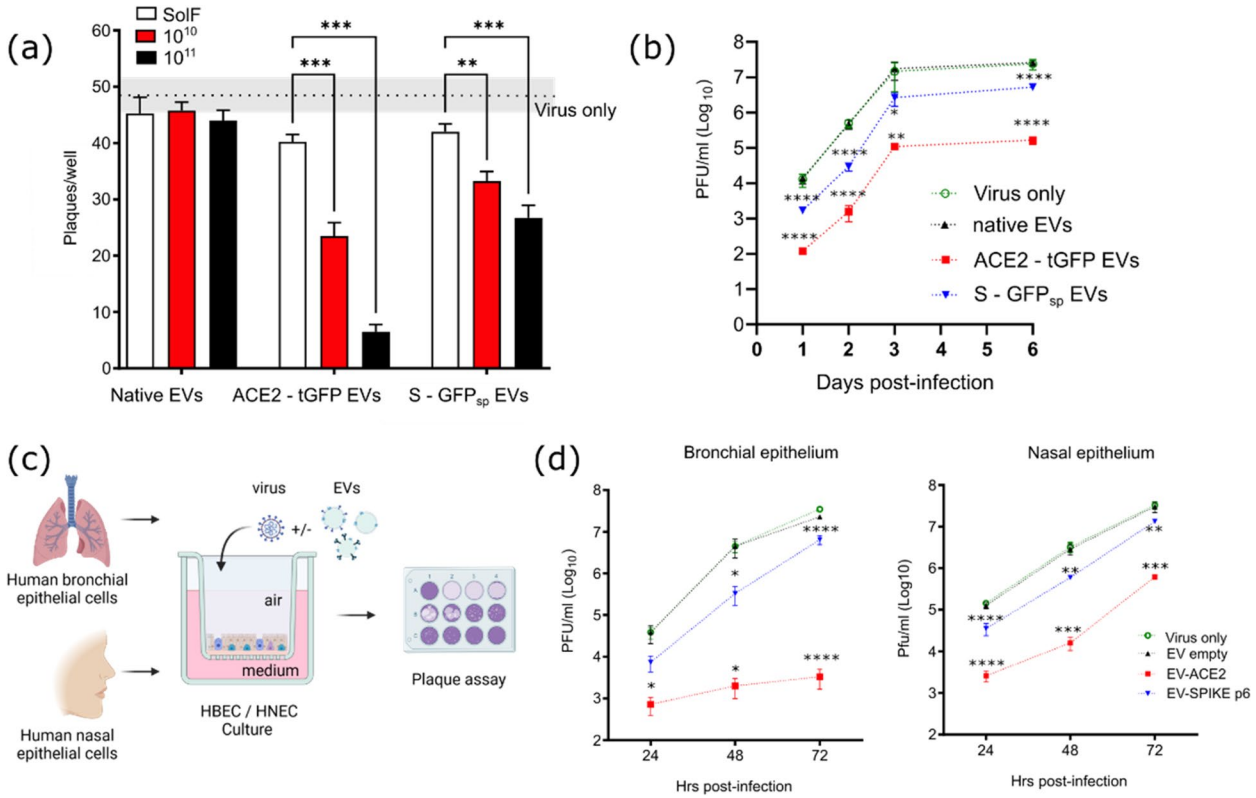

Fig. 7 Antiviral activity of native virus in different models. **a** Virus induced plaque formation in Vero cells after 1 h post-infection. The virus was either introduced alone (dashed line with grey error bars) or in combination with EV-depleted medium (SolF) as compared to the matched isolated EVs. **b** Calu-3 cells were infected with the virus in the presence or absence of EVs as indicated, for 1 h. Cell supernatant was collected 1,2,3 and 6 days post infection and virus titre was determined by a plaque-forming assay in Vero cells. **c** Cartoon illustrating the assay principle. Primary human bronchial epithelial cells (HBEC) from lung explants or human nasal epithelial cells (HNEC) were cultivated in a transwell air–liquid interface (ALI). These cells were apically infected with the virus in presence or absence of EVs. At different timepoints post-infection, 100 µl of saline solution was added apically to collected the virus for subsequent plaque assay determination of virus titres in Vero cells. Plaque forming units (PFU)/ml for the different engineered EVs are shown in **d**. Statistics: *, **, *** and ****indicate a p value of < 0.1, < 0.01, < 0.001 and < 0.0001 respectively, as calculate in a two way ANOVA test with multiple comparisons using the Dunnett correction

frequency than the infected untreated control (Fig. 8, bottom panel).

As variants with increased affinity to ACE2 and increased stability have emerged during the ongoing spread of SARS-CoV-2 over the past years, we investigated whether ACE2-tGFP EVs were still active against major VoCs and whether the S-GFP$_{sp}$ EVs exposing the Wuhan Spike remained active against the VoCs with mutated Spike proteins. ACE2-tGFP EVs maintained their anti-viral activity against the variants that emerged from February 2020 to November 2021 (D614G, Alpha, Beta, Gamma, Delta; Fig. 9a). A significant antiviral activity across these variants was also maintained with the treatment of infected Calu-3 cells with the S-GFP$_{sp}$ EVs. Surprisingly, however, ACE2-tGFP EV treatment proved entirely ineffective against the infection of Calu-3 cells with the Omicron BA.1 variant (Fig. 9a, bottom left panel). Instead, we observed a small but significant enhancement of viral replication at the dose of 10^{11}/ml ACE2-tGFP EVs. Interestingly no such loss of activity was observed for the ACE2 EVs in the PV assay (Fig. 6a, middle panel). In contrast to the ACE2-EVs, S-GFP$_{sp}$ EVs maintained activity against Omicron BA.1. When challenged with SARS-CoV-1, as expected, the Wuhan Spike exposed on the EVs did not effectively compete, at least at the low percentage of S-positive EVs and decoration stoichiometries resulting from current engineering strategies. These results were corroborated in the model using airway epithelial cells from bronchial and nasal explants. Once more, only Spike EVs, but not ACE2 EVs showed significant inhibition of Omicron replication

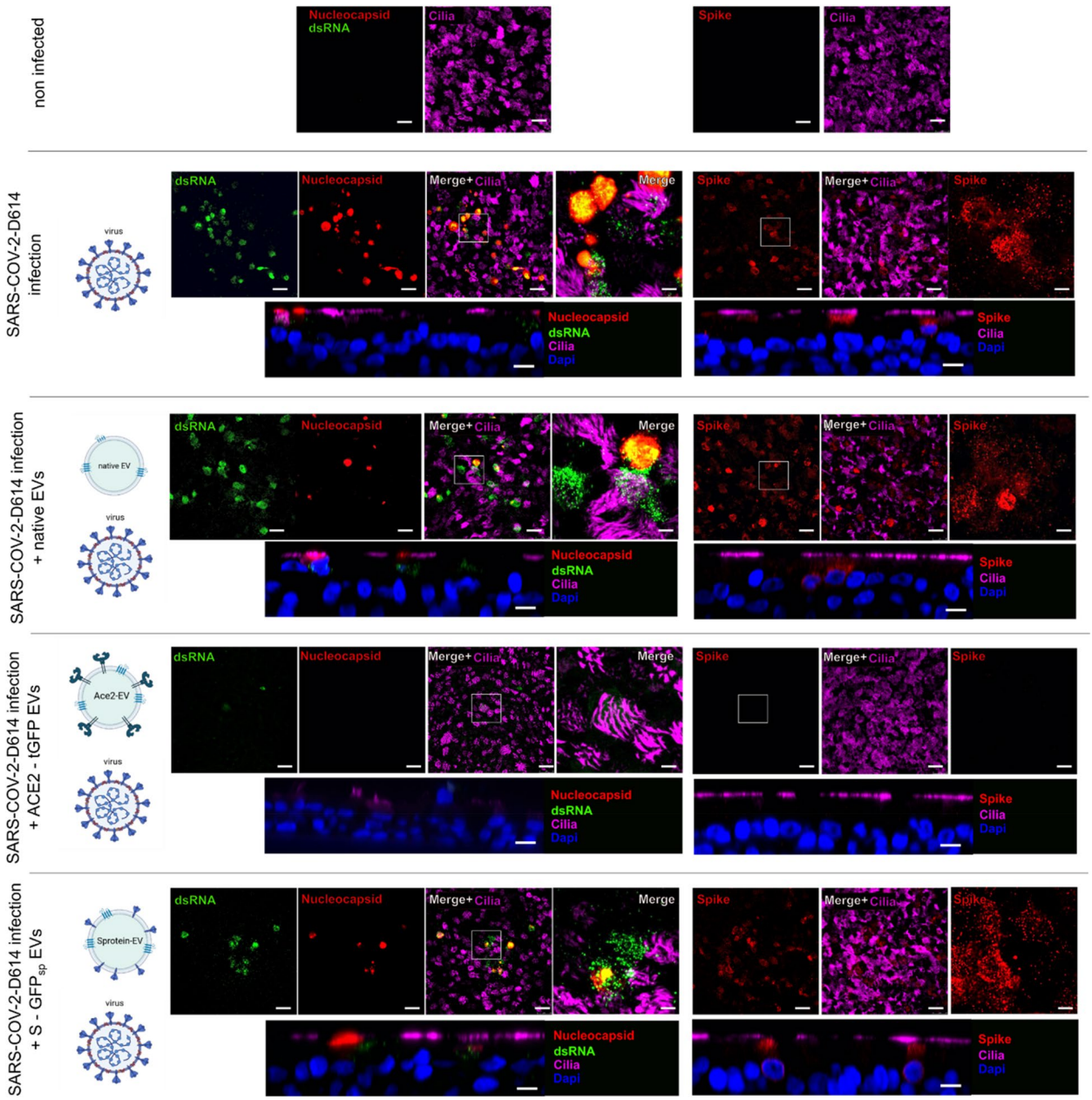

Fig. 8 ICC characterisation on bronchial explants treated with different EVs and virus. Representative immunofluorescence images of the bronchial 3D culture model as illustrated in Fig. 7c. Blue: DAPI; Green: J2 anti-dsRNA; Red (left panel): anti- SARS-CoV2-nucleocapsid protein; Red (right panel): anti-SARS-CoV-2 Spike protein; Purple: anti-acetylated tubulin (Cilia). Scale bars: 250 µm for the overview images, 50 µm for the zoom ins of the merged images and 10 µm for the xz-projections

(Fig. 9b and Supplementary Fig. 8a). Representative images from immunofluorescence of Omicron BA.1 infected HBEC cultures with different EV treatments against viral nucleocapsid and dsRNA are shown in Fig. 9c and Supplementary Fig. 8b, reaffirming the data from the plaque formation assay.

Since this drastic difference between the effect of ACE2-EVs on Omicron as compared to earlier variants was unexpected, we finally investigated whether the repeatedly reported escape of Omicron to alternative cell entry routes [33, 50] might play a role. Since Omicron can additionally switch to a TMPRSS2 independent, endosomal uptake route utilizing Cathepsin L for cleavage of the S1 subunit to mediate membrane fusion, we first tested whether this was also the case in our model. Calu-3 cells were treated for one hour with

Camostat or E64D at 10 uM and 100 uM followed by exposure to the D614G or Omicron variants of SARS-CoV-2 for another hour, and viral infectivity was measured 72 h later based on Plaque formation in Vero cells (Fig. 10a and Supplementary Fig. 9c). Consistent with previous reports, also in our Calu-3 model D614G was efficiently inhibited by the TMPRSS2 inhibitor Camostat but not susceptible to E64D treatment, indicating that Cathepsin proteases play no relevant role for its entry under these conditions. Tested side by side, within the same experiments we observed that also Omicron was strongly inhibited by Camostat, although full inhibition required higher concentrations of the compound than for inhibition of D614G. Largely consistent with previous studies [33, 50], we also observed some inhibition of Omicron by the Cathepsin inhibitor E64D which- although statistically significant- showed only ~25% inhibition at 100 µM in our model, thereby revealing that under these conditions Omicron can use alternative proteases for cell entry, but indicates that TMPRSS2 remains essential for effective infection. ACE2-EVs again inhibited D614G strongly and did not show any additive effect in combination with Camostat, which was expected given that they should hit the same pathway. E64D did not change the inhibitory effect of the ACE2-EVs on D614G, indicating that the vesicles do not alter the cell entry route of this viral strain (Fig. 10a, left panel). In contrast, for Omicron we again observed that ACE2-EVs did not inhibit, but even slightly -yet significantly- increased infectivity. Interestingly, in combination with the inhibitors we observed two effects for ACE2-EVs on Omicron: The increase of infectivity mediated by the vesicles was inhibited by E64D, supporting that the previously raised concept that EVs can serve as 'Trojan horses' for viruses, shuttling them into endosomes [53]. After 10 µM Camostat treatment, the same trend of a small increase of viral infectivity in presence of the ACE2 EVs was observed as without inhibitor, however the difference was not significant. Interestingly however, the overall uptake of Omicron in presence of ACE2-EVs remained strongly susceptible to Camostat with a smaller effect of E64D. This demonstrates that the bulk entry (> 99%) of Omicron in presence of ACE2-EVs remained TMPRSS2 dependent, thereby indicating that the ACE2-EVs – despite shuttling additional viral particles into the cells – do not entirely switch their overall protease usage and thereby preferred cell entry route.

Discussion

The converging biology between viruses and extracellular vesicles has raised interest in their application as antiviral agents or vaccines. The possibility to expose membrane proteins in their native conformation, together with avidity and entropy-based gains in binding affinity may allow to generate highly potent inhibitors of virus-receptor binding. In addition, the similar physicochemical properties of EVs and viruses highlight the potential for similar in vivo targeting. In this study, we directly compare, for the first time, two strategies aimed at inhibition of SARS-CoV entry into target cells by using EVs exposing either the ACE2 receptor or the Spike protein of the Wuhan first viral isolate on their surface. The vesicles were characterised systematically and quantitatively down to the single-vesicle level using a wide array of biochemical and imaging-based techniques. Both types of engineered EVs, designed to either act as decoy or compete with the virus, were then directly compared for inhibition of all major viral variants using a combination of relevant models, including a pseudovirus assay as well as infection with the live virus in cell lines and primary human bronchial and nasal explant models.

Related studies have primarily relied on bulk characterisation of the engineered EVs such as detection of S-protein or ACE2 by western blotting within the EV samples [8, 27, 65]. However, it is now understood that the majority of EV isolation protocols tend to co-purify non-vesicular components, thereby complicating the interpretation of these ensemble averaging data [65, 68]. Direct evidence, quantification and characterisation of *bona fide* Spike- or ACE2 decorated EV populations at the single vesicle level is thus still very limited. Our

(See figure on next page.)

Fig. 9 Effect of antiviral EVs on different SARS-CoV-2 variants in cellular and bronchial explant models. **a** Calu-3 cells were infected with different SARS-CoV-2 virus variants emerging from 2020- 2022 (D614G, Alpha, Beta, Gamma, Delta, Omicron) or SARS-CoV-1 in the presence or absence of EVs as indicated. EV depleted soluble Fraction (dashed bars) from the different EV preparations isolated during UF were used as control. White: virus only; Grey: native EVs; Blue: S – GFP_{sp} EVs; Red: ACE2 – tGFP EVs. Cell supernatant was collected 72 h after the 1 h virus/EV treatment and virus titre were determined in a plaque forming assay in Vero cells. **b** Inhibition of SARS-CoV-2 Omicron replication in the human bronchial and nasal explant model described in Fig. 5c. **c** Immunofluorescence of Omicron infected HBECs for the different treatments with and without EVs at 72 h post-infection. Blue: DAPI; Green: J2 anti-dsRNA; Red (left panel): anti- SARS-CoV2-nucleocapsid protein; Red (right panel): anti-SARS-CoV-2 Spike protein; Purple: anti-acetylated tubulin (Cilia). Scale bars: 250 µm for the overview images, 50 µm for the zoom ins of the merged images and 10 µm for the xz-projections. Statistics: *, **, *** and ****indicate a *p* value of < 0.1, < 0.01, < 0.001 and < 0.0001 respectively, as calculate in a two-way ANOVA test with multiple comparisons using the Dunnett correction

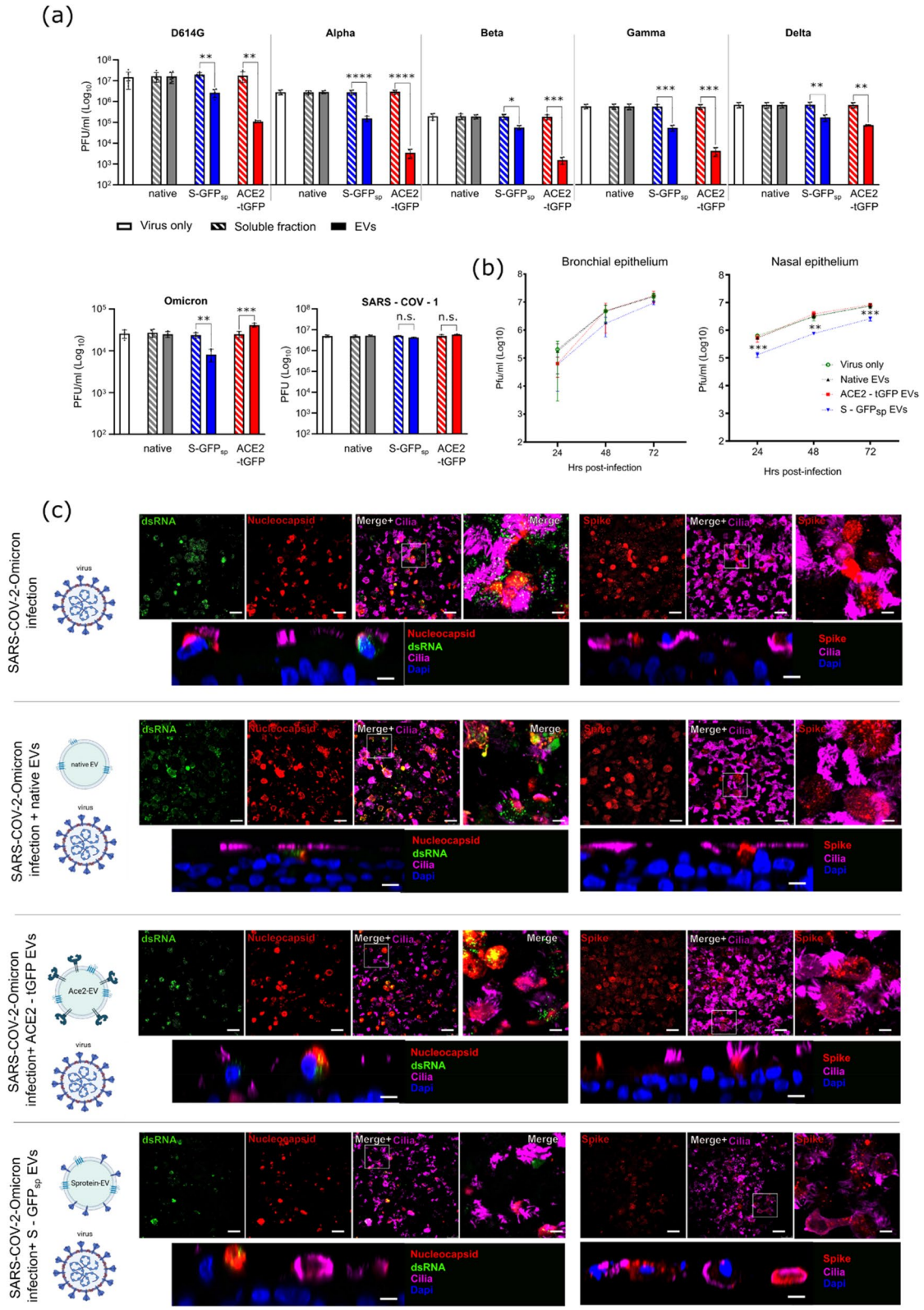

Fig. 9 (See legend on previous page.)

data show that upon transient overexpression of both, Spike- as well as ACE2- fluorescent protein reporters within HEK293T cells, there is indeed a small fraction of free Spike-protein as well as ACE2 protein secreted that does not co-fractionate with EVs. Therefore, caution is required when drawing conclusions about the mere presence of secreted proteins within EV samples on the presence and levels of engineered EVs.

Using quantitative single vesicle imaging and the EVAnalyzer plugin [48], we further provide direct evidence that the majority of secreted Spike protein and ACE2 is indeed derived from EVs decorated with these proteins. For S-GFP$_{sp}$ EVs, we were additionally able to confirm the Spike protein accessibility to antibodies in the serum of COVID-19 patients, even within the complex and protein rich environment in serum, thereby ruling out shielding by a potential protein corona being formed. Interestingly, both types of engineered EVs represented only a minor fraction of the total EV population. In particular, the Spike-positive EVs did not exceed yields of 5%, whereas ACE2 EVs reached up to 20% of all detected EVs. These vesicles were predominantly positive for CD9 as well as CD81, indicating that they primarily derive from the plasma membrane, with only a smaller contribution of CD63 positive, multivesicular body derived exosomes. While this is consistent with the intrinsic plasma membrane localisation of ACE2, the low yields of CD63 positive Spike EVs is surprising, since the S-GFP$_{sp}$ fusion protein localised not only to the plasma membrane but additionally also to MVBs and other intracellular compartments. Interestingly and in line with this result, a recent proteomics study has demonstrated that upon overexpression of S-GFP$_{sp}$, the overall population of released EVs was characterised by unchanged relative levels of CD9 and CD81 but lower amounts of CD63 as compared to matched EV samples from non-transfected cells [7]. This indicates that Spike expression might alter the host cell's vesicle biogenesis, driving it towards preferential secretion of microvesicles over exosomes. The same study reported yields of ca 25% Spike-positive EVs using Nano-flow cytometry; however, this quantification may be biased towards the engineered, fluorescent EVs which, in flow cytometry, are more sensitively detected than the scatter-based detection of the total population that is subject to a size-based detection threshold. Also, for our samples, higher fractions of ACE2- as well as Spike-positive EVs were indeed detected by Nano-flow cytometry as compared to the single vesicle imaging analysis. In contrast, the latter was purely based on fluorescence detection for both, engineered and non-engineered vesicles using either GFP-tagging versus fluorescence labelling of all proteinaceous particles by NHS chemistry, respectively. Thereby, all vesicles or particles are detected based on brightness rather than size, which allows to detect also small vesicles, beyond the ca 40–50 nm thresholds of NTA or flow cytometry. This highlights the challenge to directly compare absolute numbers from different studies and indicates that the yields of engineered EVs are indeed in the low percent range. A previous study aiming at SARS-CoV-1 vaccine development have reported increased yields of S-protein decorated EVs when replacing the transmembrane domain of the SARS-CoV-1 Spike protein with that of VSV-G [28]. In our study, applying the same engineering strategy to the SARS-CoV-2 S-protein did not result in an increase of Spike-EVs irrespective of the transmembrane domain, as assessed by quantitative single vesicle imaging and analytical size exclusion chromatography. However, the study on SARS-CoV-1 Spike EVs has quantified yields indirectly via total levels of Spike protein secreted and co-isolated with EVs by ultracentrifugation rather than a determination of truly EV associated protein. Therefore, it cannot be excluded that the higher levels of secreted chimeric Spike-VSV-G protein reported in [28] could reflect both, vesicular but also non-vesicular contributions, thereby reinforcing the need for single vesicle analytics. Additionally, also removal of the ERGIC localisation domain did not increase the yields of S-EVs despite dramatically altering the subcellular localisation. We therefore conclude that modulating the subcellular localisation might not be a straightforward strategy to enhance Spike protein loading into extracellular vesicles,

(See figure on next page.)

Fig. 10 Relevance of TMPRSS2 versus Cathepsin for SARS-CoV-2 variants in presence of ACE2-EVs. **a** Calu-3 cells were seeded and treated with Camostat or E64D for one hour at different concentrations followed by exposure to the virus with or without ACE2- tGFP EVs for another hour. Viral titres were determined after 72 h in the supernatant using a plaque forming assay in Vero cells. Percentages of viral inhibition were calculated by normalization to the virus treatment alone, bars represent averages ± SD from 4 wells, individual values are additionally shown as single spots (two independent experiments with duplicates each). Non-normalised data with absolute PFU counts are shown in Supplementary Fig. 9c. Statistics: One-way Anova with Holm-Šídák corrected multiple comparison. **b** Cartoon illustrating the different effects of ACE2-EVs on viral entry for different SARS-CoV-2 VoCs. ACE2-EVs effectively inhibit viral entry by competition with ACE2 on the cell surface. This inhibition is lost for Omicron, potentially explained by the lack of bivalent receptor binding and thereby lower stability/higher off rates of the Spike-ACE2 complex (upper panel). Additionally, Omicron can switch to an alternative entry route via endosomal Cathepsin protease cleavage, which can be additionally enhanced by the ACE2-EVs ('Trojan horse' model, bottom panel)

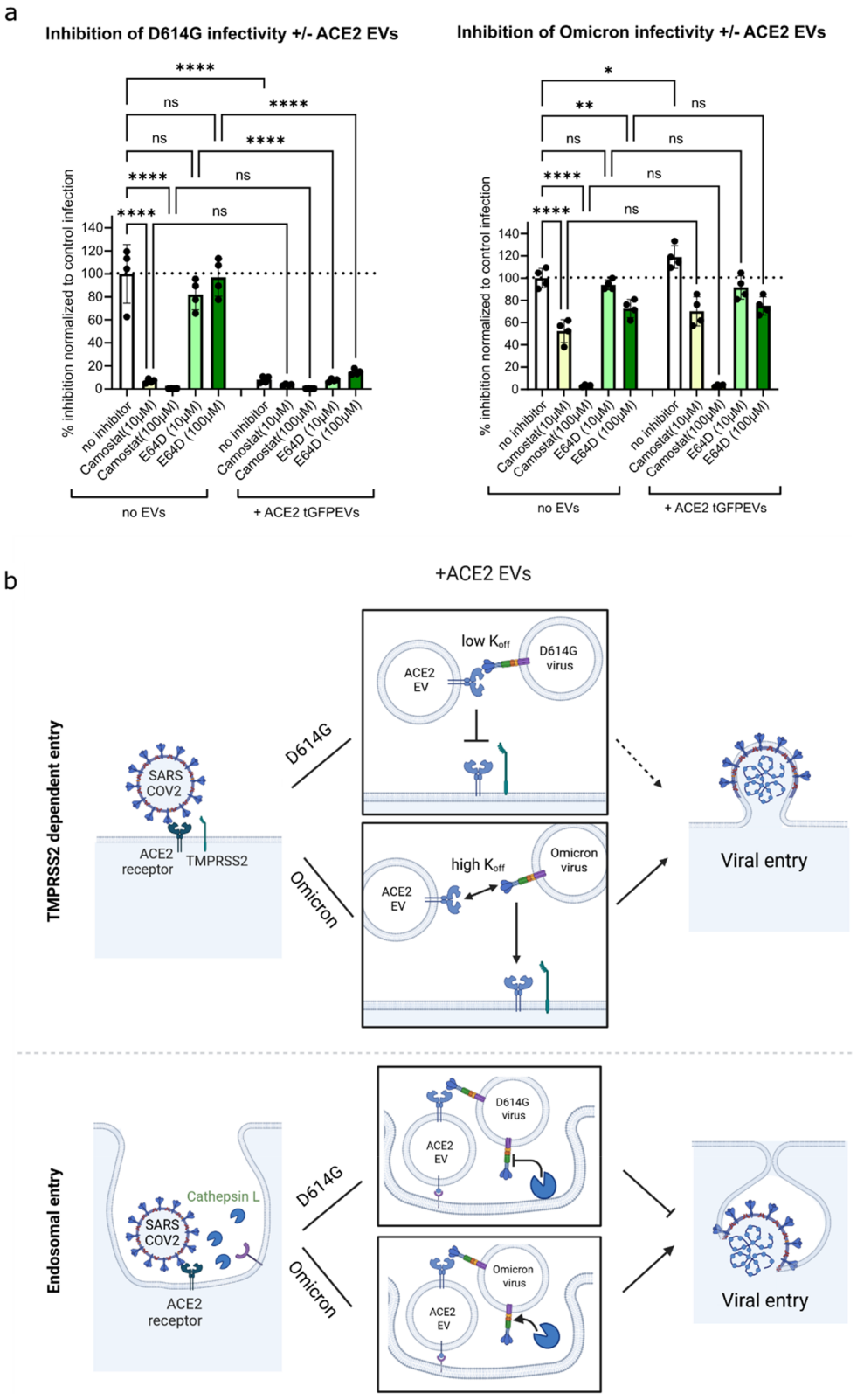

Fig. 10 (See legend on previous page.)

whereas increasing the total expression levels using e.g. stable rather than transient overexpression [57] could provide a simple solution for further investigation.

As anticipated, both types of engineered EVs inhibited infection with SARS-CoV-2 in various models in a dose dependent manner and was specific for the EVs displaying Spike or ACE2, since no inhibition was observed for either native EVs or EV depleted medium. Immunohistological detection of viral RNA and protein within bronchial explant models, as well as the kinetics of viral replication was consistent with an inhibition by both types of EVs at the stage of viral cell entry. Interestingly however, comparing the two strategies across different SARS-CoV-2 variants of concern up to the Omicron strain, resulted in several unexpected findings:

First, testing of the same antiviral EVs in the pseudovirus model did not entirely replicate the results obtained with the live viruses. While EVs carrying the spike protein were not able to prevent viral uptake, but even increased infectivity when challenged against pseudoviruses carrying the D614G, Omicron or SARS-COV-1 spike, the same spike-EVs reduced infectivity in all live virus variants of SARS-COV-2. ACE2-EVs on the other hand showed potent reduction of viral uptake in all tested pseudovirus variants (D614G, Omicron and SARS-COV-2) while in the live virus ACE2-EVs were only potently inhibiting replication of early SARS-COV-2 VOCs (from D614G to Delta) but entirely lacked any inhibition of Omicron or SARS-COV-1. The pseudovirus assay is a valuable, easy-to-use and robust tool with simplified readouts (luciferase of GFP) well suited for quick screens. As it does not reflect the entire viral life cycle it is primarily designed to monitor the initial step of viral infection and therefore widely used to quantify and benchmark potencies of viral entry inhibitors, where results for neutralising antibodies and sera can be well translated to the live virus [24]. Therefore also for our study, we conclude that the benchmarking of ACE2 EV potency against WHO standards gives a good indication for future dosing considerations.

However, our results support the importance of additionally using infection models with live viruses for studying more complex mechanisms, even though in this study the antiviral vesicles were originally also designed to simply target the initial step of viral entry. Additionally to the lack of replication competencies, the pseudovirus also differs in membrane composition, as unlike SARS-COV-2 viruses, that are formed by incorporation of the viral proteins at the ER membrane prior to lysosomal exocytosis [52], lentiviruses used for the pseudovirus production are derived from membrane budding [36] resulting in differences like increased infectivity of the pseudovirus over the live virus [47]. Since our data indicate that the conformational dynamics, sterics and likely also stoichiometries of both spike and ACE2 as well as the proteases on the three membranes (vesicles, viral particles and host cell membrane) are crucial for the inhibition or lack thereof, such differences between pseudoviral and viral particles may explain the differential results.

Second, although the Spike-EVs were engineered with the initial, less affine variant of the Spike protein from the Wuhan strain, they generally retained and even increased their inhibition potency across all SARS-CoV-2 variants, including those with enhanced affinity to the ACE2 receptor. To assess the relevance of Spike-ACE2 affinity on both infectivity and EV inhibition, we correlated our data with the dissociation constant (Kd) values for ACE2 binding by the different Spike variants, as experimentally determined in three different recent publications ([20, 30, 32]). As shown in Supplementary Fig. 9a (left panel), cellular infectivity (indicated by the number of PFU in Calu-3 cells under identical conditions and MOI, data from Fig. 9a) of different SARS-CoV-2 strains generally increased with increasing affinity/decreasing Kd of the SARS-CoV variants. Assuming a diffusion limited interaction, and an on-rate of the virus of $k_{on} \sim 1\times$ 10e8 M^{-1} s^{-1} in analogy to diffusion rates previously reported for similarly sized extracellular vesicles [72], and a Kd ranging from 1 to 30 nM (Supplementary Fig. 10a), this would result in off rates between $k_{off} \sim$ 0.1 s^{-1} to 3 s^{-1}. With $t1/2 = 0.693/k_{off}$, the half-life of the different S-ACE2 complexes can thus be estimated to range between ~0.2 to 7 s. Receptor internalisation kinetics is typically much slower with rate constants on the minute timescale [45]. A viral particle may therefore bind and dissociate many times before being internalised, whereas the longer-lived the virus-receptor complex and consequently the virus residency on the cell surface, the higher the chance for cell entry. Therefore, it is indeed plausible that changes in virus – receptor—binding affinities at the nanomolar Kd scale and thus changes in virus-receptor complex half-lives at the second scale are directly relevant for the infectivity of the virus, in particular at low MOI.

Counter-intuitively, however, the relative (percent) inhibition of Wuhan Spike-EVs against SARS-CoV-2 variants *increased* rather than decreased with the affinity gain of the Spike protein for new VoCs (Supplementary Fig. 9a). This can most likely be explained by the fact that EV concentrations were ca 10^4–10^5 times higher than virus titres (10^{10}–10^{11} EVs/well or 5×10^8–5×10^9 S-EVs/well versus an MOI of 1 for $5*10^4$ cells/well). As illustrated in Supplementary Fig. 9b, due to the massive excess of EVs over virus, under these conditions the inhibition will be approximating saturation irrespective of

the relative affinities for all viral variants, and thus result in similar absolute numbers of residual viral entry for all VoCs. This consequently results in a higher relative inhibition for high infectivity, and a lower relative inhibition for lower infectivity of different viral strains.

Third and most importantly, ACE2-EVs, while similarly potent across different VoCs up to the Delta variant, completely lost their inhibition activity for Omicron in the primary bronchial and nasal cell model, and even slightly increased the Omicron virus load in Calu-3 cells (Fig. 9a and Fig. 10a). Interestingly, it has been described that Omicron diverges from the previous SARS-CoV-2 variants in bypassing the ACE2 and TMPRSS2 dependent plasma membrane entry through an alternative endocytic route that also depends on ACE2 binding but uses endosomal proteases such as cathepsin for Spike cleavage, membrane fusion and endosomal release [63]. Since EVs are entering cells themselves though endocytosis of intact vesicles showing several hallmarks converging with viral cell entry [21, 56, 67], and since ACE2-EVs are designed to bind to the virus, it is thus conceivable that ACE2-EVs can take the bound viruses along as they are efficiently taken up themselves when exposed to cells—a concept that has repeatedly been raised for different viruses as 'Trojan horse' analogy, where viral components are either transferred within EVs [1], which has been also discussed for SARS-CoV-2 [15, 53] or where virus is dragged along with the EVs [53]. Due to the need for endosomal protease cleavage to then release the viral genome, this may result in non-functional cell entry for strictly TMPRSS2 dependent viruses, whereas such EV mediated endosomal uptake may provide a viable alternative infection route for variants which can utilise endosomal proteases. As we have observed that ACE2-EVs can increase infectivity of Omicron but not any of the other VoCs, our data would support this hypothesis. However, as this contributes only a minor addition to the viral cell entry, this does not explain the lack of Omicron inhibition- in particular since Omicron keeps using ACE2 and TMPRSS2 as major cell entry route in absence and presence of the ACE2-EVs. The main question that remains therefore elusive and warrants future investigation is why cell entry is efficiently inhibited by ACE2-EVs for all SARS-CoV-2 VoCs except Omicron. One plausible explanation may be related to the different conformational dynamics of the Omicron Spike protein compared to earlier variants. Three Spike protein chains assemble to form a homo-trimeric protein, but the conformation of the individual subunits within a trimer differs despite identical amino acid sequence. Specifically, the ACE2 receptor binding domain (RBD) can adopt a"down"or an"up"conformation, whereas only the RBD-up subunit is able to bind the ACE2 receptor. In the apo state, i.e. not in complex with ACE2, the spike of Omicron [74] is predominantly found in the one-RBD-up, two-RBD-down conformation. This is similar for the other spike variants such as Beta or Delta which are preferentially in the one-RBD-up, two-RBD-down or in the three-RBD-down conformation in the apo state [4, 71, 73].

A substantial difference is however comprised within the conformational dynamics upon ACE2 binding. Alpha, Beta, Gamma and Delta variants all undergo significant conformational transitions after ACE2 binding, resulting either in a two-RBD-up or a three-RBD-up conformation [76]. By stark contrast, the Omicron Spike protein preferentially remains in the one-RBD-up, two-RBD-down conformation even after ACE2 binding. This conformational difference translates into a dramatic consequence on the dynamics of the interaction. For all variants except Omicron, the bivalent binding mode upon synergistic binding of the second RBD subunit within one Spike trimer potentiates the affinity, directly resulting in a reduced off-rate. In contrast, for Omicron, the interaction remains monovalent and transient. Since ACE2 on the vesicles dynamically competes with ACE2 on the host cell membrane, any viral particle dissociating from an EV has the chance to rebind either of these ACE2 molecules; As binding to the cell surface will result in cleavage and internalization, viral particles are repeatedly removed from the equilibrium. The higher off-rates of Omicron Spike from the ACE2 on the vesicles would therefore less effectively compete with binding to the cell, thereby explaining why ACE2 EVs are not effective in preventing viral uptake through its major route (Fig. 10b). Resolving this mechanism in depth however will require detailed investigation of the three-dimensional confirmations, accessibilities, steric properties and dynamics between ACE2 on the vesicle, spike on the virus and TMPRSS2 on the cell surface for the different VOCs.

It has been demonstrated that, in the course of an infection as well as upon vaccination, both Spike-EVs [2, 3, 15, 44, 54] as well as ACE2-EVs [14, 71, 73], are being formed. Spike-EVs are secreted either by infected cells or cells expressing the Spike protein targeted by mRNA vaccines, whereas ACE2-EVs secreted from a variety of cells are generally found in the circulation but elevated after SARS-CoV-2 infection [14]. Previous studies have demonstrated that Spike-EVs can decoy anti-viral antibodies [54], and it has been proposed that they can contribute to secondary viral spreading from infected cells by acting as Trojan horse for viral RNA [15]—both of which can fuel the course of the infection. Based on our data, Spike-EVs may also have an opposing function, potentially competing with the virus and thus potentially dampening the infection. It is unclear how virus:EV ratios may shift with viral replication, or whether they remain constant,

as higher viral load and consequently higher S-protein expression may lead to increased release of Spike-EVs. Thus, it is an open question to what extent such auto-inhibition by competition between S-EVs and viruses both released from the infected cells may contribute to the outcome of an infection. Spike-EVs produced after vaccination could potentially also contribute to both, anti-viral antibody production by presenting and spreading antigenic viral protein, but also themselves act as anti-viral competitors. To assess these opposing roles and their contributions, it remains to be investigated how long after the initial vaccination or virus exposure such Spike-EVs may still be present in the circulation, what their titres are and how they distribute and spread within the body. ACE2-EVs produced during the SARS-CoV-2 infection on the other hand were primarily reported to counteract the virus by acting as decoy, which is also in line with our data. However, our data also reveal that this may only hold true for variants which are preferentially cleaved by plasma membrane proteases and that ACE2-EVs could in fact further promote viral spread of variants such as Omicron which can use endosomal proteases by shuttling them into EV-mediated endosomal cell entry. Likewise, the same consequences need to be considered when developing antiviral therapeutics based on engineered EVs. Based on our data and in light of current literature, we conclude that Spike-decorated EVs may provide a viable therapeutic route across variants of concern, limiting viral infection by both, direct competition with viral cell entry and potentially additionally contributing to raising anti-Spike antibodies. Other than anticipated, our data showed that the Spike-EV competitors retain their efficacy even for viral strains with improved Spike-ACE2 affinity, at least under conditions when EVs are in excess over viral particles. Therefore, the main question will be whether sufficient EV exposure can be achieved within the relevant tissues for effective competition, in particular at the onset of infection and against high affinity variants. In addition, it remains to be tested whether a potential decoy of anti-viral antibodies by the Spike protein on the EVs may counteract the beneficial function in the course of the infection. Due the evolutionary pressure for Spike protein to retain or even gain affinity to the ACE2 receptor, it would have been plausible to assume that ACE2-EV decoy may provide a strategy that can be applied for all viral variants, and thus an attractive platform for pandemic preparedness. However, based on our data, caution needs to be taken since with convergence between EV and virus cell uptake and trafficking, decoy-EVs may also serve as shuttles for the virus into alternative uptake routes and thereby enhance rather than inhibit viral spread.

Abbreviations

SARS – CoV-2	Severe Acute Respiratory Syndrome Coronavirus 2
COVID-19	Coronavirus Disease 2019
ACE2	Angiotensin Converting Enzyme 2
RBD	Receptor Binding Domain
TMPRSS2	Transmembrane Protease Serin 2
mAb	monoclonal Antibodies
VoC	Variants of Concern
shACE2	soluble human ACE2
EV	Extracellular Vesicles
ACE2-EVs	Extracellular Vesicles with Angiotensin Converting Enzyme 2
S- EVs	Extracellular Vesicles with Spike proteins
GFP	Green Fluorescent Protein
n-COV	native COV
tGFP	turbo Green Fluorescence Protein
GFPsp	Green Fluorescent Protein spark
TM	Transmembrane
VSV-G	Vesicular Stomatitis Virus G-Protein
ERGIC	Endoplasmic Reticulum Golgi-Intermediate Compartment
EMEM	Eagle's Minimum Essential Medium
FBS	Foetal Bovine Serum
DMEM	Dulbecco's Modified Eagle's Medium
HEK	Human Embryonic Kidney
HBEC	Human Bronchial Epithelial Cells
ALI	Air-Liquid Interface
hNECs	human Nasal Epithelial Cells
ACOV2	Elecsys Anti-SARS-CoV-2
ECLIA	Electrochemiluminescence Immunoassay
sVNT	surrogate Virus Neutralization Test
UF	Ultrafiltration
CM	Conditioned Medium
PBS	Phosphate Buffer Saline
NTA	Nanoparticle Tracking Analysis
NGS	Normal Goat Serum
DAD	Diode Array Detector
ONI	Oxford Nanoimager
dStorm	direct Stochastic optical reconstruction microscopy
APD	Avalanche Photodiodes
SSC	Side Scatter
FCM	Flow Cytometry
NanoFCM	High sensitivity Flow Cytometry for Nanoparticle Analysis
PI	Post-Infection
MOI	Multiplicity Of Infection
BSL-3	Biosafety Level 3
PFU	Plaque Forming Units
RT	Room Temperature
TEM	Transmission Electron Microscopy
kd	Dissociation constant
CI	Confidence Interval
FP	Fluorescent Protein
CHO	Chinese Hamster Ovary
SolF	Soluble Fraction

Supplementary Information

The online version contains supplementary material available at https://doi.org/10.1186/s12964-025-02223-x.

Supplementary Material 1.

Acknowledgements

We kindly thank Dr. Andre Görgens and Dr. Samir ElAndaloussi (Karolinska Institute, Stockholm, Sweden) for providing stable CD63-mNeon expressing HEK293T cells.

Authors' contributions

NMK and EV conceived the study. Unless specified otherwise, MS and IP carried out all experiments under guidance by NMK and EV. MS and NMK wrote the manuscript, with contributions by IP, EV and MN. All authors proofread and

commented on the manuscript. EK designed the expression constructs which were cloned by CK, NM and EK. EVs were isolated by HMB and MS, electron microscopy images were acquired by MaSt, WB analysis was performed by HMB as well as EE. Superresolution imaging was performed by MS in collaboration with MW and DS, Nano-FCM was carried out by LP. Patient sera were collected and characterised by SLP, CG and KS and provided for immunereactivity tests with the EVs, which were carried out by MS. All other EV characterisation and cellular imaging experiments were performed by MS. Pseudovirus experiments were carried out by MMN under guidance by NT. All experiments with live SARS-CoV viruses were performed by IP in the laboratory of and under guidance by EV. AV and LJVG performed immunofluorescence analysis of infected bronchial epithelia. NP and VC established cultures of bronchial epithelial cells. JB assessed the data in relation to the conformational dynamics of the spike-ACE2 complex for different SARS-COV VoCs.

Data availability

No omics datasets were generated or analysed during the current study.

Declarations

Competing interests

The authors declare no competing interests.

Author details

[1]Chemical Biology and Biological Therapeutics, Department of Biosciences and Medical Biology, Paris Lodron University Salzburg, Salzburg, Austria. [2]Viral Pathogenesis and Biosafety Unit, Division of Immunology, Transplantation, and Infectious Diseases, IRCCS San Raffaele Scientific Institute, Milan, Italy. [3]Ludwig Boltzmann Institute for Nanovesicular Precision Medicine at the Paris Lodron University Salzburg, Salzburg, Austria. [4]GMP Laboratory, Paracelsus Medical University Salzburg, Salzburg, Austria. [5]Viral Pseudotype Unit, Medway School of Pharmacy, University of Kent, Canterbury, UK. [6]Department of Translational Medical Sciences, Telethon Institute of Genetics and Medicine, University of Napoli"Federico II,"Naples, Pozzuoli, Italy. [7]UOC Genetica Medica, IRCCS Istituto Giannina Gaslini, Genova, Italy. [8]Department for Transfusion Medicine, University Hospital of Salzburg, Salzburg, Austria. [9]Cell Therapy Institute, Paracelsus Medical University, Salzburg, Austria. [10]EvoBiotiX SA, Lugano, Switzerland.

Received: 17 May 2024 Accepted: 28 April 2025
Published online: 02 July 2025

References

1. Altan-Bonnet N. Extracellular vesicles are the Trojan horses of viral infection. Curr Opin Microbiol. 2016;32:77–81. https://doi.org/10.1016/j.mib.2016.05.004.
2. Bansal S, Perincheri S, Fleming T, Poulson C, Tiffany B, Bremner RM, Mohanakumar T. Cutting Edge: Circulating Exosomes with COVID Spike Protein Are Induced by BNT162b2 (Pfizer-BioNTech) Vaccination prior to Development of Antibodies: A Novel Mechanism for Immune Activation by mRNA Vaccines. J Immunol. 2021;207(10):2405–10. https://doi.org/10.4049/jimmunol.2100637.
3. Barberis E, Vanella VV, Falasca M, Caneapero V, Cappellano G, Raineri D, Ghirimoldi M, De Giorgis V, Puricelli C, Vaschetto R, Sainaghi PP, Bruno S, Sica A, Dianzani U, Rolla R, Chiocchetti A, Cantaluppi V, Baldanzi G, Marengo E, Manfredi M. Circulating Exosomes Are Strongly Involved in SARS-CoV-2 Infection. Front Mol Biosci. 2021;8: 632290. https://doi.org/10.3389/fmolb.2021.632290.
4. Cai Y, Zhang J, Xiao T, Lavine CL, Rawson S, Peng H, Zhu H, Anand K, Tong P, Gautam A, Lu S, Sterling SM, Walsh RM Jr, Rits-Volloch S, Lu J, Wesemann DR, Yang W, Seaman MS, Chen B. Structural basis for enhanced infectivity and immune evasion of SARS-CoV-2 variants. Science. 2021;373(6555):642–8. https://doi.org/10.1126/science.abi9745.
5. Cao L, Goreshnik I, Coventry B, Case JB, Miller L, Kozodoy L, Chen RE, Carter L, Walls AC, Park YJ, Strauch EM, Stewart L, Diamond MS, Veesler D, Baker D. De novo design of picomolar SARS-CoV-2 miniprotein inhibitors. Science. 2020;370(6515):426–31. https://doi.org/10.1126/science.abd9909.
6. Cele, S., Jackson, L., Khoury, D. S., Khan, K., Moyo-Gwete, T., Tegally, H., San, J. E., Cromer, D., Scheepers, C., Amoako, D. G., Karim, F., Bernstein, M., Lustig, G., Archary, D., Smith, M., Ganga, Y., Jule, Z., Reedoy, K., Hwa, S. H., . . . Sigal, A. (2022). Omicron extensively but incompletely escapes Pfizer BNT162b2 neutralization. Nature. 602(7898), 654–656. https://doi.org/10.1038/s41586-021-04387-1
7. Choi D, Khan N, Montermini L, Tawil N, Meehan B, Kim DK, Roth FP, Divangahi M, Rak J. Quantitative proteomics and biological activity of extracellular vesicles engineered to express SARS-CoV-2 spike protein. J Extracell Biol. 2022;1(10): e58. https://doi.org/10.1002/jex2.58.
8. Cocozza F, Nevo N, Piovesana E, Lahaye X, Buchrieser J, Schwartz O, Manel N, Tkach M, Thery C, Martin-Jaular L. Extracellular vesicles containing ACE2 efficiently prevent infection by SARS-CoV-2 Spike protein-containing virus. J Extracell Vesicles. 2020;10(2): e12050. https://doi.org/10.1002/jev2.12050.
9. Corso G, Heusermann W, Trojer D, Gorgens A, Steib E, Voshol J, Graff A, Genoud C, Lee Y, Hean J, Nordin JZ, Wiklander OPB, El Andaloussi S, Meisner-Kober N. Systematic characterization of extracellular vesicle sorting domains and quantification at the single molecule - single vesicle level by fluorescence correlation spectroscopy and single particle imaging. J Extracell Vesicles. 2019;8(1):1663043. https://doi.org/10.1080/20013078.2019.1663043.
10. Cox, M., Peacock, T. P., Harvey, W. T., Hughes, J., Wright, D. W., Consortium, C.-G. U., Willett, B. J., Thomson, E., Gupta, R. K., Peacock, S. J., Robertson, D. L., & Carabelli, A. M. SARS-CoV-2 variant evasion of monoclonal antibodies based on in vitro studies. Nat Rev Microbiol. 2023;21(2):112–24. https://doi.org/10.1038/s41579-022-00809-7.
11. Dar GH, Mendes CC, Kuan WL, Speciale AA, Conceição M, Görgens A, Uliyakina I, Lobo MJ, Lim WF, El Andaloussi S, Mäger I, Roberts TC, Barker RA, Goberdhan DCI, Wilson C, Wood MJA. GAPDH controls extracellular vesicle biogenesis and enhances the therapeutic potential of EV mediated siRNA delivery to the brain. Nat Commun. 2021;12(1):6666. https://doi.org/10.1038/s41467-021-27056-3. Erratum in: Nat Commun. 2021;12(1):7357. https://doi.org/10.1038/s41467-021-27700-y.
12. Dhama, K., Khan, S., Tiwari, R., Sircar, S., Bhat, S., Malik, Y. S., Singh, K. P., Chaicumpa, W., Bonilla-Aldana, D. K., & Rodriguez-Morales, A. J. (2020). Coronavirus Disease 2019-COVID-19. Clin Microbiol Rev. 33(4). https://doi.org/10.1128/CMR.00028-20
13. Di Genova, C., Sampson, A., Scott, S., Cantoni, D., Mayora-Neto, M., Bentley, E., Mattiuzzo, G., Wright, E., Derveni, M., Auld, B., Ferrara, B. T., Harrison, D., Said, M., Selim, A., Thompson, E., Thompson, C., Carnell, G., & Temperton, N. (2021). Production, Titration, Neutralisation, Storage and Lyophilisation of Severe Acute Respiratory Syndrome Coronavirus 2 (SARS-CoV-2) Lentiviral Pseudotypes. Bio Protoc. 11(21), e4236. https://doi.org/10.21769/BioProtoc.4236
14. El-Shennawy, L., Hoffmann, A. D., Dashzeveg, N. K., McAndrews, K. M., Mehl, P. J., Cornish, D., Yu, Z., Tokars, V. L., Nicolaescu, V., Tomatsidou, A., Mao, C., Felicelli, C. J., Tsai, C. F., Ostiguin, C., Jia, Y., Li, L., Furlong, K., Wysocki, J., Luo, X., . . . Liu, H. (2022). Circulating ACE2-expressing extracellular vesicles block broad strains of SARS-CoV-2. Nat Commun. 13(1), 405. https://doi.org/10.1038/s41467-021-27893-2
15. Elrashdy F, Aljaddawi AA, Redwan EM, Uversky VN. On the potential role of exosomes in the COVID-19 reinfection/reactivation opportunity. J Biomol Struct Dyn. 2021;39(15):5831–42. https://doi.org/10.1080/07391102.2020.1790426.
16. Evrogen. https://evrogen.com/protein-descriptions/TurboGFP-description.pdf.
17. Fan Y, Pionneau C, Cocozza F, Boelle PY, Chardonnet S, Charrin S, Thery C, Zimmermann P, Rubinstein E. Differential proteomics argues against a general role for CD9, CD81 or CD63 in the sorting of proteins into extracellular vesicles. J Extracell Vesicles. 2023;12(8): e12352. https://doi.org/10.1002/jev2.12352.
18. Fu Y, Xiong S. Tagged extracellular vesicles with the RBD of the viral spike protein for delivery of antiviral agents against SARS-COV-2 infection. J Control Release. 2021;335:584–95. https://doi.org/10.1016/j.jconrel.2021.05.049.
19. Hamming I, Cooper ME, Haagmans BL, Hooper NM, Korstanje R, Osterhaus AD, Timens W, Turner AJ, Navis G, van Goor H. The emerging role of

ACE2 in physiology and disease. J Pathol. 2007;212(1):1–11. https://doi.org/10.1002/path.2162.
20. Han, P., Li, L., Liu, S., Wang, Q., Zhang, D., Xu, Z., Han, P., Li, X., Peng, Q., Su, C., Huang, B., Li, D., Zhang, R., Tian, M., Fu, L., Gao, Y., Zhao, X., Liu, K., Qi, J., . . . Wang, P. (2022). Receptor binding and complex structures of human ACE2 to spike RBD from omicron and delta SARS-CoV-2. Cell. 185(4), 630–640 e610. https://doi.org/10.1016/j.cell.2022.01.001
21. Heusermann W, Hean J, Trojer D, Steib E, von Bueren S, Graff-Meyer A, Genoud C, Martin K, Pizzato N, Voshol J, Morrissey DV, Andaloussi SE, Wood MJ, Meisner-Kober NC. Exosomes surf on filopodia to enter cells at endocytic hot spots, traffic within endosomes, and are targeted to the ER. J Cell Biol. 2016;213(2):173–84. https://doi.org/10.1083/jcb.201506084.
22. Hoffmann, M., Kleine-Weber, H., Schroeder, S., Kruger, N., Herrler, T., Erichsen, S., Schiergens, T. S., Herrler, G., Wu, N. H., Nitsche, A., Muller, M. A., Drosten, C., & Pohlmann, S. (2020). SARS-CoV-2 Cell Entry Depends on ACE2 and TMPRSS2 and Is Blocked by a Clinically Proven Protease Inhibitor. Cell. 181(2), 271–280 e278. https://doi.org/10.1016/j.cell.2020.02.052
23. Hunt, A. C., Case, J. B., Park, Y. J., Cao, L., Wu, K., Walls, A. C., Liu, Z., Bowen, J. E., Yeh, H. W., Saini, S., Helms, L., Zhao, Y. T., Hsiang, T. Y., Starr, T. N., Goreshnik, I., Kozodoy, L., Carter, L., Ravichandran, R., Green, L. B., . . . Baker, D. (2022). Multivalent designed proteins neutralize SARS-CoV-2 variants of concern and confer protection against infection in mice. Sci Transl Med. 14(646), eabn1252. https://doi.org/10.1126/scitranslmed.abn1252
24. Hyseni, I., Molesti, E., Benincasa, L., Piu, P., Casa, E., Temperton, N. J., Manenti, A., & Montomoli, E. (2020). Characterisation of SARS-CoV-2 Lentiviral Pseudotypes and Correlation between Pseudotype-Based Neutralisation Assays and Live Virus-Based Micro Neutralisation Assays. Viruses. 12(9). https://doi.org/10.3390/v12091011
25. Jackson CB, Farzan M, Chen B, Choe H. Mechanisms of SARS-CoV-2 entry into cells. Nat Rev Mol Cell Biol. 2022;23(1):3–20. https://doi.org/10.1038/s41580-021-00418-x.
26. Jiang, L., Driedonks, T. A. P., Jong, W. S. P., Dhakal, S., Bart van den Berg van Saparoea, H., Sitaras, I., Zhou, R., Caputo, C., Littlefield, K., Lowman, M., Chen, M., Lima, G., Gololobova, O., Smith, B., Mahairaki, V., Riley Richardson, M., Mulka, K. R., Lane, A. P., Klein, S. L., . . . Witwer, K. W. (2022). A bacterial extracellular vesicle-based intranasal vaccine against SARS-CoV-2 protects against disease and elicits neutralizing antibodies to wild-type and Delta variants. J Extracell Vesicles. 11(3), e12192. https://doi.org/10.1002/jev2.12192
27. Kim HK, Cho J, Kim E, Kim J, Yang JS, Kim KC, Lee JY, Shin Y, Palomera LF, Park J, Baek SH, Bae HG, Cho Y, Han J, Sul JH, Lee J, Park JH, Cho YW, Lee W, Jo DG. Engineered small extracellular vesicles displaying ACE2 variants on the surface protect against SARS-CoV-2 infection. J Extracell Vesicles. 2022;11(1): e12179. https://doi.org/10.1002/jev2.12179.
28. Kuate S, Cinatl J, Doerr HW, Uberla K. Exosomal vaccines containing the S protein of the SARS coronavirus induce high levels of neutralizing antibodies. Virology. 2007;362(1):26–37. https://doi.org/10.1016/j.virol.2006.12.011.
29. Laner-Plamberger, S., Lindlbauer, N., Weidner, L., Gansdorfer, S., Weseslindtner, L., Held, N., Lauth, W., Zimmermann, G., Kern, J. M., Fottinger, F., Ombres, L., Jungbauer, C., Rohde, E., & Grabmer, C. (2022). SARS-CoV-2 IgG Levels Allow Predicting the Optimal Time Span of Convalescent Plasma Donor Suitability. Diagnostics (Basel). 12(11). https://doi.org/10.3390/diagnostics12112567
30. Li, L., Liao, H., Meng, Y., Li, W., Han, P., Liu, K., Wang, Q., Li, D., Zhang, Y., Wang, L., Fan, Z., Zhang, Y., Wang, Q., Zhao, X., Sun, Y., Huang, N., Qi, J., & Gao, G. F. (2022). Structural basis of human ACE2 higher binding affinity to currently circulating Omicron SARS-CoV-2 sub-variants BA.2 and BA.1.1. Cell. 185(16), 2952–2960 e2910. https://doi.org/10.1016/j.cell.2022.06.023
31. Lontok E, Corse E, Machamer CE. Intracellular targeting signals contribute to localization of coronavirus spike proteins near the virus assembly site. J Virol. 2004;78(11):5913–22. https://doi.org/10.1128/JVI.78.11.5913-5922.2004.
32. Matthews AM, Biel TG, Ortega-Rodriguez U, Falkowski VM, Bush X, Faison T, Xie H, Agarabi C, Rao VA, Ju T. SARS-CoV-2 spike protein variant binding affinity to an angiotensin-converting enzyme 2 fusion glycoproteins. PLoS ONE. 2022;17(12): e0278294. https://doi.org/10.1371/journal.pone.0278294.
33. Meng, B., Abdullahi, A., Ferreira, I., Goonawardane, N., Saito, A., Kimura, I., Yamasoba, D., Gerber, P. P., Fatihi, S., Rathore, S., Zepeda, S. K., Papa, G., Kemp, S. A., Ikeda, T., Toyoda, M., Tan, T. S., Kuramochi, J., Mitsunaga, S., Ueno, T., . . . Gupta, R. K. (2022). Altered TMPRSS2 usage by SARS-CoV-2 Omicron impacts infectivity and fusogenicity. Nature. 603(7902), 706–714. https://doi.org/10.1038/s41586-022-04474-x
34. Monteil, V., Eaton, B., Postnikova, E., Murphy, M., Braunsfeld, B., Crozier, I., Kricek, F., Niederhofer, J., Schwarzbock, A., Breid, H., Devignot, S., Klingstrom, J., Thalin, C., Kellner, M. J., Christ, W., Havervall, S., Mereiter, S., Knapp, S., Sanchez Jimenez, A., . . . Penninger, J. M. (2022). Clinical grade ACE2 as a universal agent to block SARS-CoV-2 variants. EMBO Mol Med. 14(8), e15230. https://doi.org/10.15252/emmm.202115230
35. Monteil, V., Kwon, H., Prado, P., Hagelkruys, A., Wimmer, R. A., Stahl, M., Leopoldi, A., Garreta, E., Hurtado Del Pozo, C., Prosper, F., Romero, J. P., Wirnsberger, G., Zhang, H., Slutsky, A. S., Conder, R., Montserrat, N., Mirazimi, A., & Penninger, J. M. (2020). Inhibition of SARS-CoV-2 Infections in Engineered Human Tissues Using Clinical-Grade Soluble Human ACE2. Cell. 181(4), 905–913 e907. https://doi.org/10.1016/j.cell.2020.04.004
36. Moreira AS, Cavaco DG, Faria TQ, Alves PM, Carrondo MJT, Peixoto C. Advances in Lentivirus Purification. Biotechnol J. 2021;16(1): e2000019. https://doi.org/10.1002/biot.202000019.
37. Nolte-'t Hoen E, Cremer T, Gallo RC, Margolis LB. Extracellular vesicles and viruses: Are they close relatives? Proc Natl Acad Sci U S A. 2016;113(33):9155–61. https://doi.org/10.1073/pnas.1605146113.
38. Nunhofer, V., Weidner, L., Hoeggerl, A. D., Zimmermann, G., Badstuber, N., Grabmer, C., Jungbauer, C., Lindlbauer, N., Held, N., Pascariuc, M., Ortner, T., Rohde, E., & Laner-Plamberger, S. (2022). Persistence of Naturally Acquired and Functional SARS-CoV-2 Antibodies in Blood Donors One Year after Infection. Viruses. 14(3). https://doi.org/10.3390/v14030637
39. Oudit GY, Crackower MA, Backx PH, Penninger JM. The role of ACE2 in cardiovascular physiology. Trends Cardiovasc Med. 2003;13(3):93–101. https://doi.org/10.1016/s1050-1738(02)00233-5.
40. Pacciarini F, Ghezzi S, Canducci F, Sims A, Sampaolo M, Ferioli E, Clementi M, Poli G, Conaldi PG, Baric R, Vicenzi E. Persistent replication of severe acute respiratory syndrome coronavirus in human tubular kidney cells selects for adaptive mutations in the membrane protein. J Virol. 2008;82(11):5137–44. https://doi.org/10.1128/JVI.00096-08.
41. Pagani I, Ghezzi S, Alberti S, Poli G, Vicenzi E. Origin and evolution of SARS-CoV-2. Eur Phys J Plus. 2023;138(2):157. https://doi.org/10.1140/epjp/s13360-023-03719-6.
42. Partridge, L. J., Urwin, L., Nicklin, M. J. H., James, D. C., Green, L. R., & Monk, P. N. (2021). ACE2-Independent Interaction of SARS-CoV-2 Spike Protein with Human Epithelial Cells Is Inhibited by Unfractionated Heparin. Cells. 10(6). https://doi.org/10.3390/cells10061419
43. Pires De Souza GA, Le Bideau M, Boschi C, Wurtz N, Colson P, Aherfi S, Devaux C, La Scola B. Choosing a cellular model to study SARS-CoV-2. Front Cell Infect Microbiol. 2022;12:1003608. https://doi.org/10.3389/fcimb.2022.1003608.
44. Pocsfalvi G, Mammadova R, Ramos Juarez AP, Bokka R, Trepiccione F, Capasso G. COVID-19 and Extracellular Vesicles: An Intriguing Interplay. Kidney Blood Press Res. 2020;45(5):661–70. https://doi.org/10.1159/000511402.
45. Portales AE, Mustafa ER, McCarthy CI, Cornejo MP, Couto PM, Gironacci MM, Caramelo JJ, Perello M, Raingo J. ACE2 internalization induced by a SARS-CoV-2 recombinant protein is modulated by angiotensin II type 1 and bradykinin 2 receptors. Life Sci. 2022;293: 120284. https://doi.org/10.1016/j.lfs.2021.120284.
46. Sabanovic, B., Piva, F., Cecati, M., & Giulietti, M. (2021). Promising Extracellular Vesicle-Based Vaccines against Viruses, Including SARS-CoV-2. Biology (Basel). 10(2). https://doi.org/10.3390/biology10020094
47. Schmidt, F., Weisblum, Y., Muecksch, F., Hoffmann, H. H., Michailidis, E., Lorenzi, J. C. C., Mendoza, P., Rutkowska, M., Bednarski, E., Gaebler, C., Agudelo, M., Cho, A., Wang, Z., Gazumyan, A., Cipolla, M., Caskey, M., Robbiani, D. F., Nussenzweig, M. C., Rice, C. M., . . . Bieniasz, P. D. (2020). Measuring SARS-CoV-2 neutralizing antibody activity using pseudotyped and chimeric viruses. J Exp Med. 217(11). https://doi.org/10.1084/jem.20201181
48. Schurz, M., Danmayr, J., Jaritsch, M., Klinglmayr, E., Benirschke, H. M., Matea, C. T., Zimmerebner, P., Rauter, J., Wolf, M., Gomes, F. G., Kratochvil, Z., Heger, Z., Miller, A., Heuser, T., Stanojlovic, V., Kiefer, J., Plank, T., Johnson, L., Himly, M., . . . Meisner-Kober, N. (2022). EVAnalyzer: High content imaging for rigorous characterisation of single extracellular

vesicles using standard laboratory equipment and a new open-source ImageJ/Fiji plugin. J Extracell Vesicles. 11(12), e12282. https://doi.org/10.1002/jev2.12282
49. Scudieri P, Caci E, Bruno S, Ferrera L, Schiavon M, Sondo E, Tomati V, Gianotti A, Zegarra-Moran O, Pedemonte N, Rea F, Ravazzolo R, Galietta LJ. Association of TMEM16A chloride channel overexpression with airway goblet cell metaplasia. J Physiol. 2012;590(23):6141–55. https://doi.org/10.1113/jphysiol.2012.240838.
50. Shi G, Li T, Lai KK, Johnson RF, Yewdell JW, Compton AA. Omicron Spike confers enhanced infectivity and interferon resistance to SARS-CoV-2 in human nasal tissue. Nat Commun. 2024;15(1):889. https://doi.org/10.1038/s41467-024-45075-8.
51. SinoBiological. https://www.sinobiological.com/category/green-fluorescent-protein-gfpspark-elite#:~:text=The%20quantum%20yield%20of%20GFPSpark,%C2%AE%20is%20better%20than%20EGFP.
52. Steiner S, Kratzel A, Barut GT, Lang RM, Aguiar Moreira E, Thomann L, Kelly JN, Thiel V. SARS-CoV-2 biology and host interactions. Nat Rev Microbiol. 2024;22(4):206–25. https://doi.org/10.1038/s41579-023-01003-z.
53. Tey SK, Lam H, Wong SWK, Zhao H, To KK, Yam JWP. ACE2-enriched extracellular vesicles enhance infectivity of live SARS-CoV-2 virus. J Extracell Vesicles. 2022;11(5): e12231. https://doi.org/10.1002/jev2.12231.
54. Troyer Z, Alhusaini N, Tabler CO, Sweet T, de Carvalho KIL, Schlatzer DM, Carias L, King CL, Matreyek K, Tilton JC. Extracellular vesicles carry SARS-CoV-2 spike protein and serve as decoys for neutralizing antibodies. J Extracell Vesicles. 2021;10(8): e12112. https://doi.org/10.1002/jev2.12112.
55. Uhlen, M., Zhang, C., Lee, S., Sjostedt, E., Fagerberg, L., Bidkhori, G., Benfeitas, R., Arif, M., Liu, Z., Edfors, F., Sanli, K., von Feilitzen, K., Oksvold, P., Lundberg, E., Hober, S., Nilsson, P., Mattsson, J., Schwenk, J. M., Brunnstrom, H., . . . Ponten, F. (2017). A pathology atlas of the human cancer transcriptome. Science. 357(6352). https://doi.org/10.1126/science.aan2507
56. van Dongen HM, Masoumi N, Witwer KW, Pegtel DM. Extracellular Vesicles Exploit Viral Entry Routes for Cargo Delivery. Microbiol Mol Biol Rev. 2016;80(2):369–86. https://doi.org/10.1128/MMBR.00063-15.
57. Verta, R., Grange, C., Skovronova, R., Tanzi, A., Peruzzi, L., Deregibus, M. C., Camussi, G., & Bussolati, B. (2022). Generation of Spike-Extracellular Vesicles (S-EVs) as a Tool to Mimic SARS-CoV-2 Interaction with Host Cells. Cells. 11(1). https://doi.org/10.3390/cells11010146
58. Viana, R., Moyo, S., Amoako, D. G., Tegally, H., Scheepers, C., Althaus, C. L., Anyaneji, U. J., Bester, P. A., Boni, M. F., Chand, M., Choga, W. T., Colquhoun, R., Davids, M., Deforche, K., Doolabh, D., du Plessis, L., Engelbrecht, S., Everatt, J., Giandhari, J., . . . de Oliveira, T. (2022). Rapid epidemic expansion of the SARS-CoV-2 Omicron variant in southern Africa. Nature. 603(7902), 679–686. https://doi.org/10.1038/s41586-022-04411-y
59. Vicenzi E, Canducci F, Pinna D, Mancini N, Carletti S, Lazzarin A, Bordignon C, Poli G, Clementi M. Coronaviridae and SARS-associated coronavirus strain HSR1. Emerg Infect Dis. 2004;10(3):413–8. https://doi.org/10.3201/eid1003.030683.
60. Wan, Y., Shang, J., Graham, R., Baric, R. S., & Li, F. (2020). Receptor Recognition by the Novel Coronavirus from Wuhan: an Analysis Based on Decade-Long Structural Studies of SARS Coronavirus. J Virol. 94(7). https://doi.org/10.1128/JVI.00127-20
61. Wang, X., Chen, X., Tan, J., Yue, S., Zhou, R., Xu, Y., Lin, Y., Yang, Y., Zhou, Y., Deng, K., Chen, Z., Ye, L., & Zhu, Y. (2022). 35B5 antibody potently neutralizes SARS-CoV-2 Omicron by disrupting the N-glycan switch via a conserved spike epitope. Cell Host Microbe. 30(6), 887–895 e884. https://doi.org/10.1016/j.chom.2022.03.035
62. Wang Z, Popowski KD, Zhu D, de Juan Abad BL, Wang X, Liu M, Lutz H, De Naeyer N, DeMarco CT, Denny TN, Dinh PC, Li Z, Cheng K. Exosomes decorated with a recombinant SARS-CoV-2 receptor-binding domain as an inhalable COVID-19 vaccine. Nat Biomed Eng. 2022;6(7):791–805. https://doi.org/10.1038/s41551-022-00902-5.
63. Willett, B. J., Grove, J., MacLean, O. A., Wilkie, C., De Lorenzo, G., Furnon, W., Cantoni, D., Scott, S., Logan, N., Ashraf, S., Manali, M., Szemiel, A., Cowton, V., Vink, E., Harvey, W. T., Davis, C., Asamaphan, P., Smollett, K., Tong, L., . . . Thomson, E. C. (2022). SARS-CoV-2 Omicron is an immune escape variant with an altered cell entry pathway. Nat Microbiol. 7(8), 1161–1179. https://doi.org/10.1038/s41564-022-01143-7
64. Wolf, M., Poupardin, R. W., Ebner-Peking, P., Andrade, A. C., Blochl, C., Obermayer, A., Gomes, F. G., Vari, B., Maeding, N., Eminger, E., Binder, H. M., Raninger, A. M., Hochmann, S., Brachtl, G., Spittler, A., Heuser, T., Ofir, R., Huber, C. G., Aberman, Z., . . . Strunk, D. (2022). A functional corona around extracellular vesicles enhances angiogenesis, skin regeneration and immunomodulation. J Extracell Vesicles. 11(4), e12207. https://doi.org/10.1002/jev2.12207
65. Wu C, Xu Q, Wang H, Tu B, Zeng J, Zhao P, Shi M, Qiu H, Huang Y. Neutralization of SARS-CoV-2 pseudovirus using ACE2-engineered extracellular vesicles. Acta Pharm Sin B. 2022;12(3):1523–33. https://doi.org/10.1016/j.apsb.2021.09.004.
66. Wu F, Zhao S, Yu B, Chen YM, Wang W, Song ZG, Hu Y, Tao ZW, Tian JH, Pei YY, Yuan ML, Zhang YL, Dai FH, Liu Y, Wang QM, Zheng JJ, Xu L, Holmes EC, Zhang YZ. A new coronavirus associated with human respiratory disease in China. Nature. 2020;579(7798):265–9. https://doi.org/10.1038/s41586-020-2008-3.
67. Wurdinger T, Gatson NN, Balaj L, Kaur B, Breakefield XO, Pegtel DM. Extracellular vesicles and their convergence with viral pathways. Adv Virol. 2012;2012: 767694. https://doi.org/10.1155/2012/767694.
68. Xie F, Su P, Pan T, Zhou X, Li H, Huang H, Wang A, Wang F, Huang J, Yan H, Zeng L, Zhang L, Zhou F. Engineering Extracellular Vesicles Enriched with Palmitoylated ACE2 as COVID-19 Therapy. Adv Mater. 2021;33(49): e2103471. https://doi.org/10.1002/adma.202103471.
69. Yan R, Zhang Y, Li Y, Xia L, Guo Y, Zhou Q. Structural basis for the recognition of SARS-CoV-2 by full-length human ACE2. Science. 2020;367(6485):1444–8. https://doi.org/10.1126/science.abb2762.
70. Zhang H, Lv P, Jiang J, Liu Y, Yan R, Shu S, Hu B, Xiao H, Cai K, Yuan S, Li Y. Advances in developing ACE2 derivatives against SARS-CoV-2. Lancet Microbe. 2023;4(5):e369–78. https://doi.org/10.1016/S2666-5247(23)00011-3.
71. Zhang J, Xiao T, Cai Y, Lavine CL, Peng H, Zhu H, Anand K, Tong P, Gautam A, Mayer ML, Walsh RM Jr, Rits-Volloch S, Wesemann DR, Yang W, Seaman MS, Lu J, Chen B. Membrane fusion and immune evasion by the spike protein of SARS-CoV-2 Delta variant. Science. 2021;374(6573):1353–60. https://doi.org/10.1126/science.abl9463.
72. Zhang P, Jiang J, Zhou X, Kolay J, Wang R, Wan Z, Wang S. Label-free imaging and biomarker analysis of exosomes with plasmonic scattering microscopy. Chem Sci. 2022;13(43):12760–8. https://doi.org/10.1039/d2sc05191e.
73. Zhang, Q., Jeppesen, D. K., Higginbotham, J. N., Franklin, J. L., Crowe, J. E., Jr., & Coffey, R. J. (2021). Angiotensin-converting Enzyme 2-containing Small Extracellular Vesicles and Exomeres Bind the Severe Acute Respiratory Syndrome Coronavirus 2 Spike Protein. Gastroenterol. 160(3), 958–961 e953. https://doi.org/10.1053/j.gastro.2020.09.042
74. Zhao, Z., Zhou, J., Tian, M., Huang, M., Liu, S., Xie, Y., Han, P., Bai, C., Han, P., Zheng, A., Fu, L., Gao, Y., Peng, Q., Li, Y., Chai, Y., Zhang, Z., Zhao, X., Song, H., Qi, J., . . . Gao, G. F. (2022). Omicron SARS-CoV-2 mutations stabilize spike up-RBD conformation and lead to a non-RBM-binding monoclonal antibody escape. Nat Commun. 13(1), 4958. https://doi.org/10.1038/s41467-022-32665-7
75. Zheng W, Radler J, Sork H, Niu Z, Roudi S, Bost JP, Gorgens A, Zhao Y, Mamand DR, Liang X, Wiklander OPB, Lehto T, Gupta D, Nordin JZ, El Andaloussi S. Identification of scaffold proteins for improved endogenous engineering of extracellular vesicles. Nat Commun. 2023;14(1):4734. https://doi.org/10.1038/s41467-023-40453-0.
76. Zhou, T., Tsybovsky, Y., Gorman, J., Rapp, M., Cerutti, G., Chuang, G. Y., Katsamba, P. S., Sampson, J. M., Schon, A., Bimela, J., Boyington, J. C., Nazzari, A., Olia, A. S., Shi, W., Sastry, M., Stephens, T., Stuckey, J., Teng, I. T., Wang, P., . . . Kwong, P. D. (2020). Cryo-EM Structures of SARS-CoV-2 Spike without and with ACE2 Reveal a pH-Dependent Switch to Mediate Endosomal Positioning of Receptor-Binding Domains. Cell Host Microbe. 28(6), 867–879 e865. https://doi.org/10.1016/j.chom.2020.11.004

Publisher's Note